CHALMERS
UNIVERSITY OF TECHNOLOGY

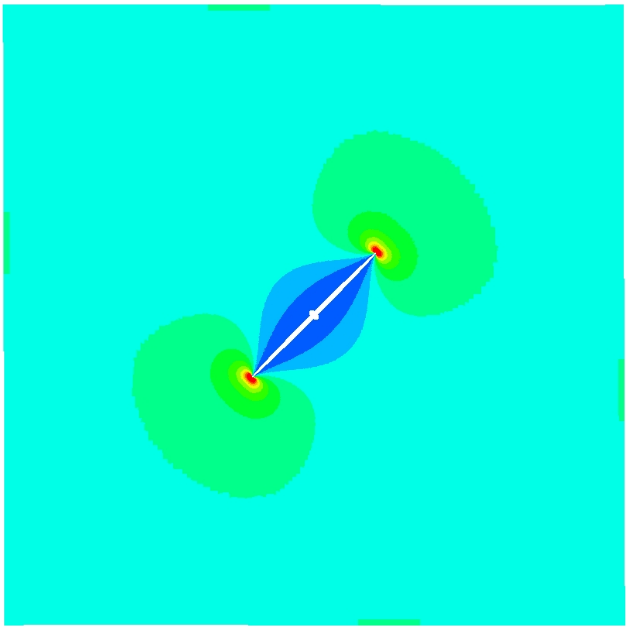

Numerical Investigation of Mixed-Mode Crack Growth

Prediction of crack growth direction, crack growth rate, and fatigue life

Master's thesis in Applied Mechanics

Fiona Coates
Maja Sunesson

DEPARTMENT OF INDUSTRIAL AND MATERIALS SCIENCE
CHALMERS UNIVERSITY OF TECHNOLOGY
Gothenburg, Sweden 2026
www.chalmers.se

MASTER'S THESIS 2026

Numerical Investigation of Mixed-Mode Crack Growth

Prediction of crack growth direction, crack growth rate, and fatigue life

Fiona Coates
Maja Sunesson

Department of Industrial and Materials Science
Division of Material and Computational Mechanics
CHALMERS UNIVERSITY OF TECHNOLOGY
Gothenburg, Sweden 2026

Numerical Investigation of Mixed-Mode Crack Growth:
Prediction of crack growth direction, crack growth rate, and fatigue life
Fiona Coates & Maja Sunesson

Supervisor: Mohammad Salahi Nezhad, FS Dynamics
Examiner: Fredrik Larsson, Department of Mechanical Engineering

Master's Thesis 2026
Department of Industrial and Material Science
Division of Material and Computational Mechanics
Chalmers University of Technology
SE-412 96 Gothenburg
Telephone +46 31 772 1000

Cover: Simulated and evaluated stress component of the RSB8 experiment.

Typeset in LaTeX
Printed by Chalmers Reproservice
Gothenburg, Sweden 2026

Numerical Investigation of Mixed-Mode Crack Growth:
Prediction of crack growth direction, crack growth rate, and fatigue life
Fiona Coates & Maja Sunesson
Department of Industrial and Material Science
Chalmers University of Technology

Abstract

Fatigue crack growth poses a critical challenge to service life of components, especially in safety-sensitive industries such as aviation and railway transportation, where structural components are subjected to millions of load cycles during service. Reliable prediction of crack growth direction and rate is essential for damage-tolerant design and maintenance planning.

Stress intensity factor-based criteria are widely used when the crack is loaded in one single mode. However, their applicability for mixed-mode crack growth under non-proportional loading conditions remains limited. The Vector Crack Tip Displacement (VCTD) criterion has been proposed in the literature as an alternative, offering advantages in generality by relying on displacement measures rather than assuming linear elastic material with small-scale yielding. However, its performance under general mixed-mode fatigue loading conditions requires further investigation.

In this study, several mixed-mode fatigue crack growth experiments from the literature are modeled within a two-dimensional Finite Element (FE) framework. The experiments include Four Point Bending, Compact Tension Shear, two variations of biaxial stress experiments, and a Twin-disc experiment. The performance of three formulations of the VCTD criterion are investigated in terms of their ability to predict crack growth direction. In addition, crack growth rate using Paris law and the resulting fatigue life are assessed independently along the predicted crack paths, and sequentially compared against experimental data from the literature.

The VCTD criterion successfully captures crack growth direction in cases where the crack propagates along a straight path, with good agreement between predicted fatigue life and experimental results from the literature. However, all three formulations consistently fail to predict abrupt changes in crack direction, such as kinking and branching behavior. The origin of this discrepancy is discussed, considering the following possible contributing factors: microstructural features that may drive kinking in the physical experiments in ways not captured by the FE model, simplifications inherent to the FE framework that may affect the displacement fields at the crack tip, and a potential fundamental limitation of the VCTD criterion itself, which may lack a mechanism to detect abrupt directional changes.

Keywords: Vector Crack Tip Displacement (VCTD), mixed-mode fatigue, crack growth direction, crack growth rate, non-proportional loading, finite element analysis, fracture mechanics.

Acknowledgements

We would like to express our sincere gratitude to FS Dynamics for the opportunity to carry out this project. In particular, we especially want to thank our supervisor Mohamad Salahi Nezhad and the FEM group manager Emina Music for their trust in our ability to carry out this project.

We are deeply grateful to our supervisors Mohammad Salahi Nezhad at FS Dynamics and Fredrik Larsson at Chalmers University of Technology, who also served as examiner and provided the alternative VCTD formulation. Their dedicated guidance, continuous support, and insightful feedback have been invaluable throughout this project, and it has been a true privilege to learn and develop under their mentorship.

Fiona Coates & Maja Sunesson, Gothenburg, May 2026

"Doing research means going from one rabbit hole to another and cherishing your achievements in between rabbit holes." - Amir Reza Khoei

List of Acronyms

Below is the list of acronyms that have been used throughout this thesis listed in alphabetical order:

CTS	Compact Tension Shear
FE	Finite Element
FPB	Four Point Bending
RCF	Rolling Contact Fatigue
VCTD	Vector Crack Tip Displacement

Nomenclature

Below is the nomenclature of symbols, parameters, and variables used throughout this thesis.

Parameters

E	Young's modulus
ν	Poisson's ratio
μ	Shear modulus
r	Radial distance from crack tip
θ	Polar angle at crack tip
d_h	Distance between crack tip nodes used in VCTD evaluation
ψ	Reversed shear threshold
T_c	Duration of load cycle
H	Heaviside step function
C	Material parameter used in Paris law
m	Material parameter used as exponent in Paris law
Δt	Time step size
h_c	Element edge length

Variables

$\Delta\mathbf{a}$	Crack driving displacement vector
$\Delta\mathbf{a}^+$	Trial crack driving displacement of presumed positive direction
$\Delta\mathbf{a}^-$	Trial crack driving displacement of presumed negative direction
$\hat{\mathbf{e}}_\perp$	Unit vector in the perpendicular direction of the crack
$\hat{\mathbf{e}}_\parallel$	Unit vector in the parallel direction of the crack
$\mathbf{u}^+$	Nodal displacement of the positive defined crack face
$\mathbf{u}^-$	Nodal displacement of the negative defined crack face

δ_I	Mode I displacement component
δ_{II}	Mode II displacement component
$\bar{\delta}_I$	Mode I mid value of displacement component
$\bar{\delta}_{II}$	Mode II mid value of displacement component
$\tilde{\delta}_I$	Mode I "amplitude" of displacement component
$\tilde{\delta}_{II}$	Mode II "amplitude" of displacement component
$\tilde{\delta}$	Crack tip displacement
f^+	Reversed shear contribution for positive defined crack face
f^-	Reversed shear contribution for negative defined crack face
ϑ	Instantaneous crack growth angle
φ	Predicted crack propagation direction
$\hat{\mathbf{e}}_\varphi$	Unit vector pertinent to the direction of crack propagation
$\hat{\mathbf{e}}_\vartheta$	Unit vector in the direction of the instantaneous growth direction
K_I	Mode I stress intensity factor
K_{II}	Mode II stress intensity factor
ΔK_I	Mode I stress intensity factor range
ΔK_{II}	Mode II stress intensity factor range
ΔK_{eq}	Equivalent stress intensity factor range
da/dN	Crack growth rate

Contents

List of Figures

List of Tables

1 Introduction

This chapter presents the introduction of this thesis by outlining the background and its purpose. In addition to the motivation, sustainability aspects are discussed. and the objective, scope and limitation of the work are presented.

1.1 Background

Fatigue is one of the most common failure mechanisms in structural components. It occurs as a result of cyclic loading and is often initiated in the presence of a pre-existing micro structural defects. Under cyclic loading, cracks can be initiated and may subsequently propagate due to repeated time-varying loading and unloading. Fatigue crack propagation occurs as the crack tip advances, and notably, cracks may continue to grow even when the applied cyclic load does not exceed the yield strength of the material [1].

Because such damage accumulates progressively and often without visible warning, fatigue poses a particular threat in various industries, especially safety-critical industries such as aviation and railway transportation. In these sectors, structural components are subjected to millions of load cycles during service, making reliable life prediction essential. In aviation structures, components such as landing gear assemblies and fuselage panels are subjected to repeated cyclic stresses during service [2]. Even critical rotating components of gas turbines, particularly aircraft turbine engine discs, are highly susceptible to fatigue failure [3]. Similarly, railway infrastructure components such as rails, axles, and welded joints undergo millions of load cycles due to repeated wheel–rail contact forces, axle loads, braking, and track irregularities [4]. Rolling Contact Fatigue (RCF) represents the most significant safety challenges in railway systems worldwide. It is responsible for a substantial proportion of rail and wheel replacements, contributing to annual costs in the hundreds of millions of euros in Europe. In addition to replacement costs, RCF contributes to a substantial number of derailments and traffic disruptions each year, leading to further economic losses and safety risks [5].

Given the importance of maintaining structural integrity, fatigue crack growth is a phenomenon that requires extensive research. From an engineering and maintenance perspective, reliable crack growth predictions capabilities are essential for preventing material failure and optimizing inspection and repairs. This requires information regarding crack initiation (when crack formation begins), crack propagation direction (in which path the crack will grow), and crack growth rate (how fast the crack propagates), all of which are critical for assessing remaining service life and ensuring safe operation. The rate of crack growth is commonly modeled using the Paris law, which relates the crack growth rate to the stress intensity factors (SIFs) [6]. Notably, crack growth rate and direction are closely coupled, as the path the crack follows directly affects the stress environment at the crack tip. In safety-critical structures, these considerations are closely related to the design philosophy adopted to ensure structural integrity.

Traditionally, two main approaches are used: the safe-life approach and the damage-tolerance approach. The safe-life approach assumes that components are removed from service before fatigue cracks can initiate, i.e., calculate fatigue life before crack initiation [7]. In contrast, the damage-tolerant approach assumes that cracks exist and therefore structures are designed for fatigue crack growth and inspection intervals are set so that cracks growth can be monitored before reaching the critical lengths and sizes [1]. In this context, accurate prediction of fatigue crack growth behavior becomes a key requirement for reliable structural design and maintenance planning.

In fracture mechanics, crack loading is commonly classified into three modes: opening (Mode I), in-plane shear (Mode II), and out-of-plane shear (Mode III) [8], see Figure 1.1. In most practical engineering applications, fatigue cracks are often subjected to mode I loadings, and therefore the majority of existing crack propagation criteria, which are typically based on SIFs, work well for this condition [9]. However, complex mixed-mode loading conditions frequently arise in components subjected to multiaxial or non-proportional loading. Under such conditions, the interactions between fracture modes significantly complicates the prediction of crack growth behavior, particularly the crack propagation direction, thereby limiting the reliability of conventional SIF-based criteria [10].

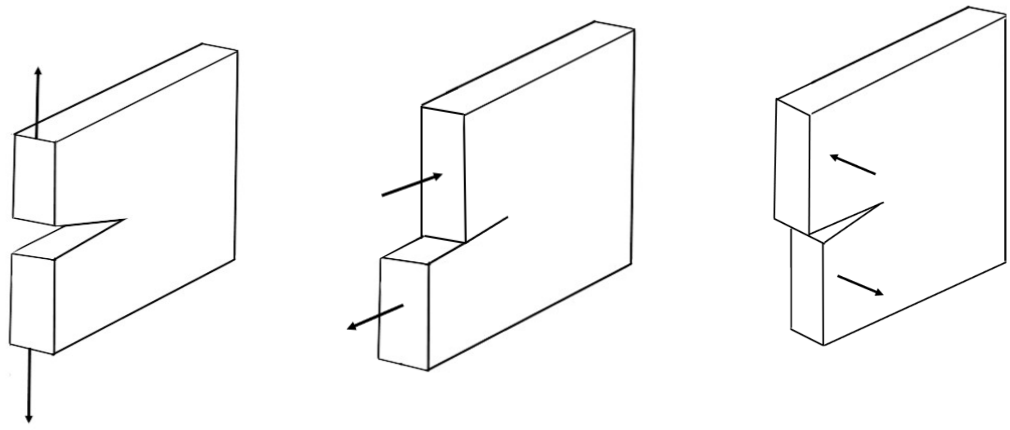

(a) **(b)** **(c)**

Figure 1.1: Different modes in fracture mechanics. (a) Mode I. (b) Mode II. (c) Mode III.

Although SIF-based approaches remain widely used for fatigue crack growth predictions, their applicability to general mixed-mode crack growth problems under non-proportional loading conditions has not yet been fully established. Extensions of the classical criteria have been proposed to account for effects such as non-proportional loading [11], crack closure, and crack face friction [12]. However, these extensions often require additional assumptions, effective parameters, or complex stress analyses, which reduce their generality.

To address some of these limitations, a criterion based on measured crack tip displacement has been proposed by Li [13], known as the Vector Crack Tip Displacement (VCTD) method. Instead of presupposing an elastic stress singularity, the VCTD criterion is not restricted to linear elastic material behavior and can be applied to arbitrary constitutive responses. Furthermore, the crack growth direction is governed by the crack tip displacement, which carries both magnitude and directional information fundamental to the deformation at the crack tip, making it particularly attractive for mixed-mode fatigue problems involving non-linearities or complex loading paths. Despite these theoretical advantages, the applicability and performance of different VCTD formulations under general mixed-mode fatigue loading conditions have not been systematically evaluated. This thesis therefore aims to assess the predictive capability of different VCTD formulations for crack growth direction and evaluate the crcak growth rate, examining both stationary and propagating crack configurations through finite element analyses of experimentally validated cases from the literature.

1.1.1 Social, Environmental and Ethical aspects

In addition to the technical aspects, it is relevant to briefly consider the broader societal, ethical, and environmental context of the work. Research on fatigue crack propagation contributes to improved safety and reliability in structural components, particularly in safety-critical applications, and may therefore have wider societal implications.

From an environmental perspective, the outcomes of this work may indirectly affect design strategies, where considerations such as resource efficiency and waste reduction are relevant. In addition, the use of computational resources should be carried out with awareness of energy consumption and its associated environmental impact.

1.2 Objective

This thesis aims to evaluate the predictive capability of different VCTD-based formulations for general mixed-mode fatigue crack growth direction, as well as evaluating the crack growth rate and the cycles to failure. Finite element analyses of experimentally validated cases from the literature are performed, covering both stationary crack configurations and propagating cracks. The primary goal is to assess the VCTD formulations ability to capture crack growth behavior under the considered mixed-mode loading conditions, and to identify their respective strengths and limitations.

1.3 Scope

The scope of this work includes numerical modeling of mixed-mode fatigue crack growth experiments drawn from the literature. Crack growth direction is evaluated at the crack tip using several VCTD formulations, for both stationary and propagating crack configurations. Fatigue life estimations are computed for each predicted crack path. Results from the simulations are compared to available experimental data in literature. All models are implemented within a two-dimensional plane stress/strain FE framework using ANSA for pre-processing [14], ABAQUS CAE for simulation [15], and MATLAB for post-processing [16].

1.4 Limitations

The following modeling assumptions and simplifications define the boundaries of this study. Material behavior is treated as linear elastic throughout, this is supported by evidence in the literature showing that elastic-plastic modeling does not meaningfully improve crack direction predictions for the considered problem class [17]. All models are two-dimensional, which excludes three-dimensional effects such as crack front curvature, out-of-plane constraints, and mode III contributions, effects that are considered secondary for the planar specimen geometries examined. Finally, the analysis is confined to crack propagation direction and rate, crack initiation is outside the scope of this work, as the focus lies on the growth behavior of pre-existing cracks.

2

Theoretical Framework

This chapter presents the theoretical framework for the analyses performed in this work. Four topics are covered, each of which can be read independently.

The first is the Vector Crack Tip Displacement (VCTD) criterion, which forms the basis for predicting general mixed-mode fatigue crack growth direction. Three formulations of the criterion are considered: one including reversed shear restrictions [17], one excluding them [18], and an alternative formulation in which the crack growth direction is governed by the rate of the crack driving displacement vector rather than its instantaneous direction.

The second and third topics concern an independent fatigue life assessment performed along the crack paths. Stress intensity factors (SIFs) are used to quantify the crack driving force near the crack tip, and the Paris law is then applied to derive two bounding estimates of the crack growth rate under mixed-mode loading, from which the total fatigue life is estimated.

Finally, the crack face contact formulation is described, which is employed in simulations where compressive loading is expected to cause partial crack closure.

2.1 Vector Crack Tip Displacement Criteria

The VCTD criterion was first introduced by Li [13]. The criterion is based on the evaluation of crack tip displacements and can be applied to materials with general constitutive behavior, where he proposed to linearly combine the Crack Tip Opening Displacement (CTOD) related to mode I fatigue cracks and Crack Tip Sliding Displacement (CTSD) related to mode II. The criterion assumes that, under mode I loading, the crack propagates along the original crack path, which corresponds to a direction approximately 45° from the direction of maximum shear stress. In contrast, when multiple slip occurs at the crack tip, shear-mode fatigue cracks are predicted to deviate from the original crack path and propagate at approximately 45° relative to the initial crack direction [13].

The VCTD criterion was further investigated by Floros et al. [17], who developed an accumulated formulation of the criterion under mixed-mode fatigue crack growth experiments and included factors such as non-proportional loading. Where the criterion is based on the distances on created by opening (δ_I) and sliding (δ_{II}) crack face discontinuities, measured at a certain distance (d_h) from the crack tip [13], as illustrated in Figure 2.1.

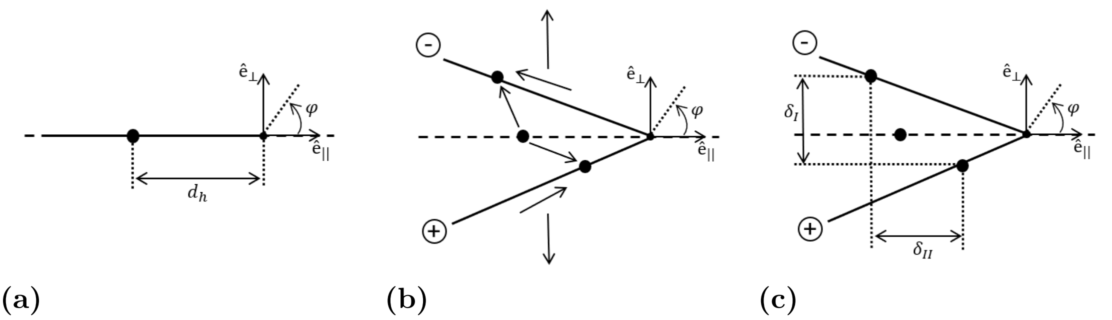

Figure 2.1: Crack geometry configurations. The dashed line indicates the undeformed crack. (a) Undeformed, closed crack. (b) Illustration of positive defined directions and angle. (c) Crack tip displacements δ_I and δ_{II}.

The unit vectors $\hat{e}_\perp$ and $\hat{e}_{||}$ lie in the perpendicular and parallel directions to the crack and defines a local coordinate system with origin at the crack tip. φ signifies the defined positive crack growth angle. The distances δ_I and δ_{II} are computed at each time instance t of the load cycle at a constant d_h as

$$\delta_I(t) = [\mathbf{u}^-(t) - \mathbf{u}^+(t)] \cdot \hat{\mathbf{e}}_\perp, \qquad \delta_{II}(t) = [\mathbf{u}^+(t) - \mathbf{u}^-(t)] \cdot \hat{\mathbf{e}}_{||}, \tag{2.1}$$

where $\mathbf{u}^-(t)$ and $\mathbf{u}^+(t)$ denote displacements of the adjacent points at the positive and negative sides of the crack, respectively, seen in Figure 2.1c.

Furthermore, a vector of the crack tip displacement can then be defined as

$$\mathbf{d}(t) = [\langle \delta_I(t) \rangle + |\delta_{II}(t)|] \cdot \hat{\mathbf{e}}_{||} + \delta_{II}(t) \cdot \hat{\mathbf{e}}_\perp. \tag{2.2}$$

In the present work, three formulations of the VCTD criterion are considered: (i) a formulation including reversed shear contributions, following Floros et al. [17], (ii) a formulation excluding reversed shear, following Salahi Nezhad et al. [18], and (iii) an alternative formulation in which the crack growth direction is determined by the rate of the crack driving displacement vector, rather than its instantaneous direction.

2.1.1 Including Reversed Shear restriction

To account for the out-of-phase loading, Floros et al. [17] proposed a modification of the original VCTD formulation. To reflect kinematic hardening effects due to local plasticity at the crack tip, the "amplitudes" of the crack face deformations are evaluated for every instance as,

$$\tilde{\delta}_I(t) = \delta_I(t) - \bar{\delta}_I, \quad \tilde{\delta}_{II}(t) = \delta_{II}(t) - \bar{\delta}_{II}. \tag{2.3}$$

Where $\bar{\delta}_I$ and $\bar{\delta}_{II}$ are the mid values over a load cycle,

$$\bar{\delta}_I(t) = \frac{1}{2}\left[\max_t \delta_I(t) + \min_t \delta_I(t)\right], \quad \bar{\delta}_{II}(t) = \frac{1}{2}\left[\max_t \delta_{II}(t) + \min_t \delta_{II}(t)\right]. \tag{2.4}$$

Following Li [13], the instantaneous crack driving displacement is defined as

$$\tilde{\delta}(t) = \sqrt{\langle\tilde{\delta}_I(t)\rangle^2 + 2\langle\tilde{\delta}_I(t)\rangle|\tilde{\delta}_{II}(t)| + 2\tilde{\delta}_{II}(t)^2}. \tag{2.5}$$

Here, $|\bullet|$ denotes the absolute value, and $\langle\bullet\rangle$ are the Macaulay brackets, $\langle\bullet\rangle = \frac{1}{2}[\bullet + |\bullet|]$. The crack driving displacement from the evaluated load cycle is then determined by

$$\Delta\mathbf{a} = \underset{\Delta\tilde{\mathbf{a}}\in\Delta\mathbf{a}^+,\Delta\mathbf{a}^-}{\arg\max} |\Delta\tilde{\mathbf{a}}|. \tag{2.6}$$

The set of trial displacement vectors for presumed positive ($\Delta\mathbf{a}^+$) and negative ($\Delta\mathbf{a}^-$) growth direction, are evaluated assuming "rate-independent" response over the entire load cycle as

$$\Delta\mathbf{a}^+ = \int_0^{T_c} \langle d_t\tilde{\delta}(t)\rangle \hat{\mathbf{e}}_\vartheta(t) f^+(t), \quad \Delta\mathbf{a}^- = \int_0^{T_c} \langle d_t\tilde{\delta}(t)\rangle \hat{\mathbf{e}}_\vartheta(t) f^-(t). \tag{2.7}$$

Where $d_t\tilde{\delta}(t) = \frac{\tilde{\delta}(t_n)-\tilde{\delta}(t_{n-1})}{t_n-t_{n-1}}$, T_c denotes the duration of the load cycle, and $\hat{\mathbf{e}}_\vartheta(t)$ is the instantaneous unit vector in the direction determined by

$$\vartheta(t) = \arcsin\frac{\tilde{\delta}_{II}(t)}{\tilde{\delta}(t)}. \tag{2.8}$$

The reversed shear contribution is determined by

$$f^+(t) = \begin{cases} 0, & \tilde{\delta}_{II} < 0 \ \ \& \ \ \frac{\delta_I}{|\delta_{II}|} \leq \psi \\ 1, & \tilde{\delta}_{II} \geq 0 \ \ \textbf{or} \ \ \frac{\delta_I}{|\delta_{II}|} > \psi \end{cases}, \quad f^-(t) = \begin{cases} 0, & \tilde{\delta}_{II} > 0 \ \ \& \ \ \frac{\delta_I}{|\delta_{II}|} \leq \psi \\ 1, & \tilde{\delta}_{II} \leq 0 \ \ \textbf{or} \ \ \frac{\delta_I}{|\delta_{II}|} > \psi \end{cases}, \tag{2.9}$$

where ψ is the reversed shear threshold parameter, used to account for crack face locking by restricting the contribution of reversed shear instances. Here, reversed shear refers to a shear deformation with the opposite sign to the presumed growth direction, following the framework introduced in [17]. Crack face locking is defined such that only the active (open) part of the crack contributes to relative crack face displacements at each time instance, for inactive crack faces in contact, no relative displacement is considered. The parameter ψ controls how strictly reversed shear contributions are restricted, and its effect can be summarized as follows:

- $\psi < 0$, would impose no restrictions on reversed shear contribution, leading to equal contribution in opposite shear directions during a load cycle would cancel out.

- $\psi = 0$, imposes restriction on reverse shear when there is active contact.
- $\psi > 0$, requires crack opening to allow for reversed shear.

In the present analyses, a value of $\psi = 0.01$ was used as the reference value for all cases. For cases involving crack face contact, an additional value of $\psi = 0.001$ was also evaluated in order to assess the sensitivity of the predicted direction to the number of reversed shear instances included in the accumulation. Both values were chosen as small positive thresholds, meaning that reversed shear is allowed to contribute only when the crack is sufficiently open.

The trial direction that results in the largest magnitude of the crack driving displacement is chosen as the preferred fatigue crack growth direction (φ), and is henceforth determined by its unit vector,

$$\hat{\mathbf{e}}_{\varphi} = \frac{\Delta\mathbf{a}}{||\Delta\mathbf{a}||}. \tag{2.10}$$

Here, $|| \bullet ||$ denotes the Euclidean norm.

2.1.2 Excluding Reversed Shear restriction

The formulation without reversed shear restriction, presented in [18], follows the same procedure as described in Section 2.1.1, with the exception that the reversed shear restriction is omitted. This leads to the functions ($f^{+/-}$), seen in Equation (2.7), to be excluded. The criterion excluding the reversed shear is described briefly below:

Using the crack face displacements are the "amplitudes" evaluated as,

$$\tilde{\delta}_{I/II}(t) = \delta_{I/II}(t) - \bar{\delta}_{I/II}, \tag{2.11}$$

$$\text{using:} \quad \bar{\delta}_{I/II}(t) = \frac{1}{2}\left[\max_t\left(\delta_{I/II}(t)\right) + \min_t\left(\delta_{I/II}(t)\right)\right]. \tag{2.12}$$

The instantaneous crack driving displacement is again evaluated as,

$$\tilde{\delta}(t) = \sqrt{\langle\tilde{\delta}_I(t)\rangle^2 + 2\langle\tilde{\delta}_I(t)\rangle|\tilde{\delta}_{II}(t)| + 2\tilde{\delta}_{II}(t)^2}, \tag{2.13}$$

The instantaneous crack growth direction, in the crack local coordinate system shown in Figure 2.1 is then computed as,

$$\vartheta(t) = \arcsin\left(\frac{\tilde{\delta}_{II}(t)}{\tilde{\delta}(t)}\right). \tag{2.14}$$

The crack driving displacement vector can then be determined using $\hat{\mathbf{e}}_{\vartheta}(t)$, which is the unit vector in the direction of the instantaneous growth direction ($\vartheta(t)$) as,

$$\Delta\mathbf{a} = \int_0^{T_c} \langle d_t\tilde{\delta}(t)\rangle\hat{\mathbf{e}}_{\vartheta}(t)dt, \tag{2.15}$$

where T_c denotes the duration of the load cycle. Finally, the crack propagation direction resulting from the full load cycle, φ, can be determined from the unit vector in the crack tip local coordinate system as,

$$\hat{\mathbf{e}}_{\varphi} = \frac{\Delta\mathbf{a}}{||\Delta\mathbf{a}||}, \tag{2.16}$$

again, $|| \bullet ||$ indicates the Euclidean norm.

2.1.3 Alternative Formulation

An alternative formulation of the VCTD criterion has been derived, in which the effects of reverse shear are once again neglected. Just as the previously described formulations, contributions to crack growth are accumulated only during the loading phase of the cycle. However, the key distinction is that the crack growth direction is governed by the rate of the crack driving displacement vector $(d(t))$, rather than its instantaneous direction $(\hat{e}_{\vartheta}(t))$.

Once again, the crack face displacements are evaluated as

$$\tilde{\delta}_{I/II}(t) = \delta_{I/II}(t) - \bar{\delta}_{I/II}, \tag{2.17}$$

$$\text{using:}\quad \bar{\delta}_{I/II}(t) = \frac{1}{2}\left[\max_t\left(\delta_{I/II}(t)\right) + \min_t\left(\delta_{I/II}(t)\right)\right], \tag{2.18}$$

where the vector of the crack tip displacement is then be defined as

$$\mathbf{d}(t) = [\langle\tilde{\delta}_I(t)\rangle + |\tilde{\delta}_{II}(t)|]\hat{\mathbf{e}}_{II} + \delta_{II}(t)\hat{\mathbf{e}}_{\perp}. \tag{2.19}$$

Whose norm is given by

$$|\mathbf{d}(t)| = \sqrt{\langle\tilde{\delta}_I(t)\rangle^2 + 2\langle\tilde{\delta}_I(t)\rangle|\tilde{\delta}_{II}(t)| + 2\tilde{\delta}_{II}(t)^2}. \tag{2.20}$$

The crack driving displacement of the load cycle is expressed as

$$\Delta\mathbf{a} = \int_0^{T_c} H(d_t|d(t)|)\ d_t\mathbf{d}\,dt, \tag{2.21}$$

where the Heaviside step function $H(x)$ is defined as

$$H(x) := \begin{cases} 1, & x \geq 0, \\ 0, & x < 0. \end{cases} \tag{2.22}$$

In this formulation, the Heaviside function acts as a loading–unloading operator. When $d_t|\mathbf{d}(t)| \geq 0$, corresponding to the loading phase, the integrand contributes to crack growth. During unloading, when $d_t|\mathbf{d}(t)| < 0$, the Heaviside function suppresses the contribution, and no additional crack driving displacement is accumulated. Furthermore as $|\mathbf{d}(t)|$ increases, the rate $d_t\mathbf{d}$ points in the direction that contributes to crack growth, so no separate unit vector needs to be defined. The crack propagation direction (φ) is now determined from the unit vector in the crack tip local coordinate system as

$$\hat{\mathbf{e}}_\varphi = \frac{\Delta\mathbf{a}}{||\Delta\mathbf{a}||}. \tag{2.23}$$

2.2 Stress Intensity Factors

In order to predict the stress state near the tip of a crack, stress intensity factors are used [19]. Their magnitude depends on the specimen geometry, as well as the size and location of the crack. It is important to note that several methods exist for evaluating SIFs. One such method utilizes the interaction integral method, which is an integral derived from the J-integral based on the superposition of two admissible solutions to a boundary value problem [20]. This method is adopted by ABAQUS, and a detailed discussion of the J-integral and how it is used to derive the SIFs are beyond the scope of this thesis, however, it is important to understand how ABAQUS evaluates the integration contours. The interaction integral is computed over a series of contours around the crack tip, each contour can be interpreted as a virtual domain surrounding the crack tip. These domains are defined by "rings" of elements extending from one crack face to the opposite crack face. The contours are constructed such that each successive contour encloses the previous one, such that the first contour consist of the crack font, and the next contour consist of the rows of elements in contact with the first contour as well as the elements of the previous contour, and so on, this is visualized by Figure 2.2. In principle, the evaluated SIFs should be independent of the chosen contour, therefore, multiple contours are used to assess the consistency and accuracy of the results.

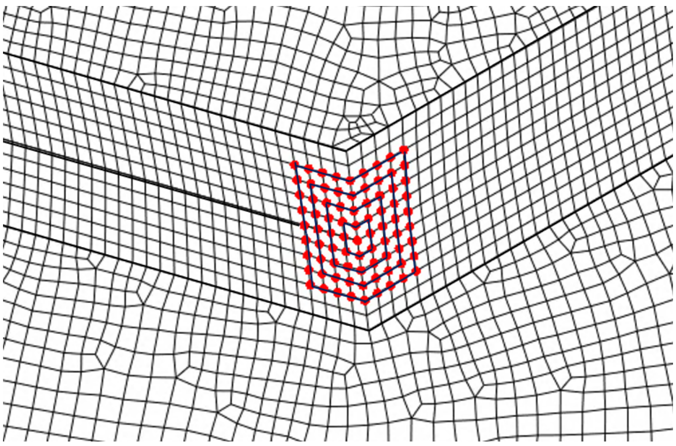

Figure 2.2: Example of the contours defined by ABAQUS for an arbitrary mesh.

Note that no matter which method used in order to determine the stress intensity factors, the ranges between the SIFs are still calculated the same way [19]

$$\Delta K_I(d_h) = \max_t(K_I(d_h, t)) - \max_t(0, \min_t(K_I(d_h, t))), \tag{2.24}$$

$$\Delta K_{II}(d_h) = \max_t(K_{II}(d_h, t)) - \min_t(K_{II}(d_h, t)). \tag{2.25}$$

The range ΔK_I accounts for crack closure effects by disregarding the compressive portion of the mode I cycle, since a closed crack does not contribute to crack driving. Mode II, by contrast, is evaluated over its full range, as sliding displacements can occur regardless of crack opening status.

2.3 Crack Growth Rate

A commonly used relation for fatigue crack growth rate is Paris law, $da/dN = C(\Delta K)^m$, where C and m are material parameters [6]. To account for the non-proportionality of the loads, two bounding estimates of the crack growth rate are considered, following the work of Salahi Nezhad et al. [18], reflecting different assumptions about how mode I and mode II interact.

The lower estimate assumes that the two modes are applied sequentially and act independently, so that the total growth rate is simply the sum of their individual contributions [21]:

$$\frac{da}{dN} = C(\Delta K_I)^m + C(\Delta K_{II})^m. \tag{2.26}$$

The upper estimate is to consider the loading of the modes simultaneously applied. The equivalent driving force (ΔK) is then derived from energy considerations [1], yielding

$$\frac{da}{dN} = C(\Delta K_{eq})^m \quad \text{where:} \quad \Delta K_{eq} = \sqrt{(\Delta K_I)^2 + (\Delta K_{II})^2} \tag{2.27}$$

An important practical aspect of fatigue calculations is to predict the remaining fatigue life of the component until a specific crack size. This can be done by integrating predicted crack growth rates assuming linear variation of the growth between two consecutive data points.

2.4 Crack Face Contact

To represent a realistic crack and prevent unphysical interpenetration of crack faces under compressive loading, a penalty contact formulation [22] has been implemented in simulations where crack face contact is expected. However, crack face friction is neglected. The contact pressure is related to the penetration through

$$p_n = -\epsilon_n g_n \quad \text{for} \quad g_n < 0, \tag{2.28}$$

where ϵ_n is the penalty parameter and g_n is the gap between the crack faces, with g_n <0 indicating penetration. The penalty parameter governs the stiffness of the contact constraint, where a higher value of ϵ_n reduces penetration. Unless stated otherwise, ϵ_n was set to the default value provided by ABAQUS, in which the parameter is derived from a representative stiffness of the elements on either side of the crack face [15].

3

Assessment of Crack Growth Behavior

This chapter presents a numerical assessment of mixed-mode fatigue crack growth experiments reported in the literature. The main objective is to evaluate how different formulations of the Vector Crack Tip Displacement (VCTD) criterion predict crack propagation direction, and crack path evolution, under different combinations of mode I and mode II loading. Crack growth rates are also evaluated under such conditions. The assessment is intentionally divided into two levels. First, the criteria are evaluated along experimentally observed crack paths. This provides a local verification of whether the crack tip displacement field at a known crack geometry gives the experimentally observed growth direction. Second, the crack is propagated incrementally by only using the directions predicted by the selected VCTD formulation. This provides a more realistic numerical simulation of the experiment, since the predicted crack path is no longer prescribed by the experiment.

The overall workflow adopted for each experiment is illustrated in Figure 3.1, and consists of five main stages: literature review and model definition, Finite Element (FE) model development, numerical simulation, post-processing for crack propagation direction and growth rate predictions, and finally a comparison with available data in the literature.

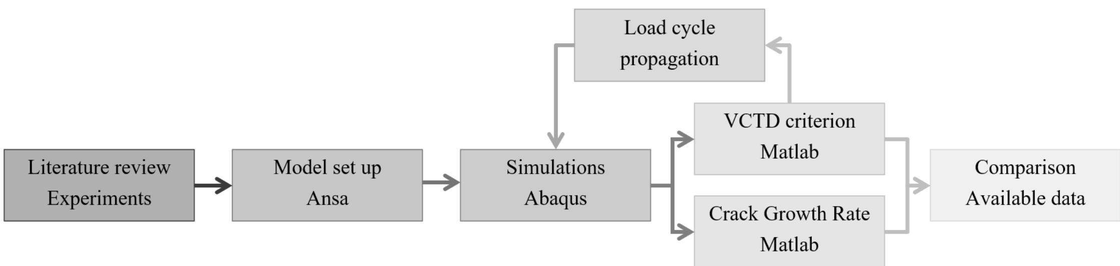

Figure 3.1: Visualization of the project workflow.

In the first stage, the relevant experimental information was extracted from the literature, including specimen geometry, material properties, loading conditions and boundary conditions. FE models were subsequently created in ANSA, including geometry definition, mesh generation, applied loads, and crack geometry. The models were solved in ABAQUS using linear elastic simulations under time-varying loading. For each load cycle, crack tip field quantities required to evaluate the VCTD criterion were extracted, together with the Stress Intensity Factors (SIFs). Post-processing was performed in MATLAB, where the extracted crack tip displacements were used to predict crack growth direction, while the SIFs were used to estimate crack growth rates and fatigue life according to the formulations presented in Chapter 2.

Two numerical strategies are used throughout the chapter. In the first strategy, stationary cracks are introduced at successive locations along the measured experimental crack path. The crack geometry is therefore known in advance, and the criterion is only required to reproduce the local direction of propagation at each evaluated crack tip position. This approach is useful for assessing whether the VCTD criterion gives a physically reasonable local direction when the correct crack geometry is already present.

In the second strategy, the crack is advanced incrementally in the direction predicted by the employed VCTD criterion. In this case, the crack path is not prescribed by the experiment. Any error in the predicted direction modifies the subsequent crack geometry, and consequently also the future crack tip displacement field, SIF history and crack growth rate estimate. The propagated path simulations are therefore a stricter investigation of the predictive capability of the criterion.

Finally, the predicted crack propagation directions, crack paths, and growth rates were compared against experimental data and results published in the literature, if available.

The experiments investigated in this chapter are: Four Point Bending (FPB), Compact Tension Shear (CTS), two biaxial stress experiments (RSB8/RSB3), and Twindisc. Each experiment is presented in a dedicated section, introduced with a description of the experimental setup, followed by the FE model configuration, and concluding with the obtained numerical results.

3.1 Four Point Bending

The first validation case was the asymmetric Four Point Bending (FPB) experiment performed by Qian and Fatemi [9]. The experimental configuration is shown in Figure 3.2. This case is useful as a baseline because the crack is initially subjected to mixed-mode loading, but the subsequent crack path is predominantly governed by mode I opening.

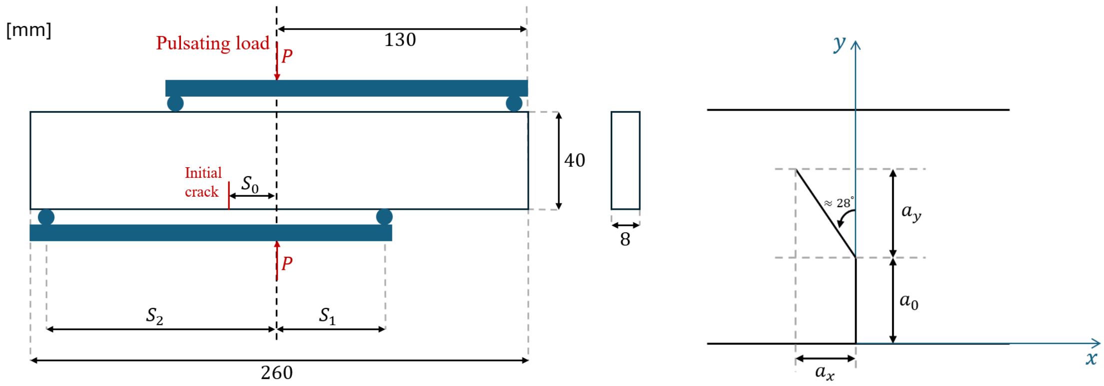

(a) **(b)**

Figure 3.2: Experimental setting of FPB used by Qian and Fatemi [9]. (a) Dimensions and load configuration. (b) Final crack configuration.

The beam was pre-cracked under pure mode I loading, creating a vertical crack with length of 11.91 mm. A pulsating load (P) was then applied on the beam through two simply supported plates at the top and bottom of the beam, with the crack positioned off center, creating an asymmetric four point bending configuration. The initial stress intensity ratio (K_{II}/K_I) experienced by the pre-existing crack depends on the relative position of the crack with respect to the applied load. While pure FPB produces a constant bending moment region, the asymmetric positioning of the crack relative to the loading points introduces a non-zero shear force at the crack tip. This results in a simultaneous opening (mode I) and sliding (mode II) deformation of the crack faces. In this case, a ratio of $K_{II}/K_I = 0.262$ was examined, which corresponds to a mode I dominant mixed-mode loading condition. The beam was made out of SAE 1045 hot rolled and normalized steel, and the specimen surface were well polished, for which $E = 202$ GPa and $\nu = 0.29$ are presumed in accordance to Dowling [1].

The experiment resulted in an almost straight fatigue crack with an angle of $\varphi \approx 28°$. The local crack path direction (φ) is measured as the positive counterclockwise angle from the y-axis, as indicated in Figure 3.2b. The experimental conditions are summarized in Table 3.1.

Table 3.1: Test conditions of FPB used by Qian and Fatemi [9]

Initial K_{II}/K_I	Initial crack length [mm]	S_0 [mm]	S_1 [mm]	S_2 [mm]	P_{max} [kN]	P_{min} [kN]	Final crack length a_x [mm]	a_y [mm]	Cycles to failure
0.262	11.91	21	40	120	14.3	0.89	7.39	13.48	208 900

3.1.1 FE setup

The FPB experiment was modeled using a linear elastic plane stress material. Plane stress conditions were assumed because the specimen thickness is small compared with the in-plane dimensions, consistent with the modeling assumptions in [9]. The specimen was modeled as a simply supported beam, where the lower-left support was constrained in the vertical direction, while the lower-right support was constrained in both the vertical and horizontal directions to prevent rigid body motion. The external force (P) is applied according to the reaction forces of the supporting beam in the experimental setup. The FE setup is shown in Figure 3.3.

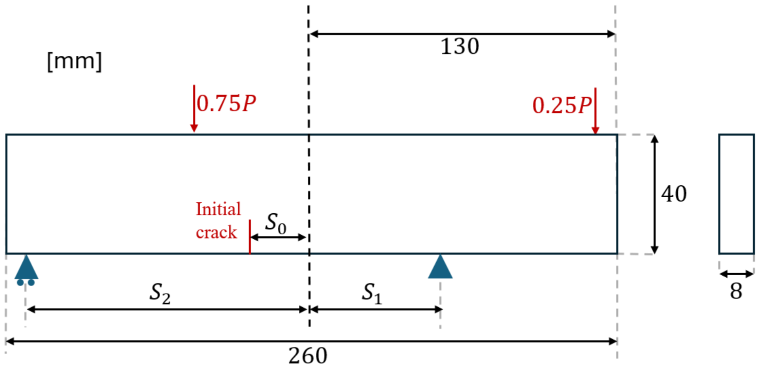

Figure 3.3: Visualization of FPB FE setup.

The dimensions are the same as for the experimental setup, presented in Table 3.1. In order to replicate the pulsating load applied in the experiment, a sinusoidal load configuration was applied in the simulations to represent the cyclic nature of fatigue loading in the experiment, shown in Figure 3.4.

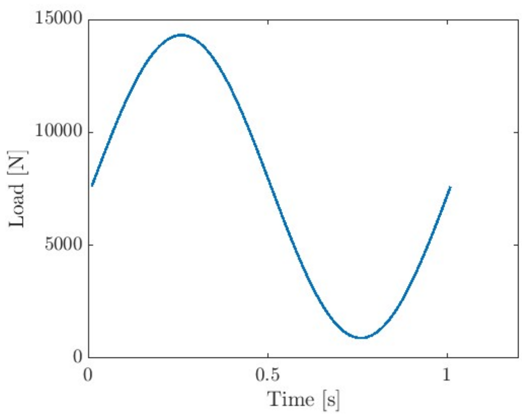

Figure 3.4: Employed sinusoidal load variation in FPB experiment.

Since fatigue crack growth is governed by the time variation of loading over a cycle rather than the absolute load level, it is essential to resolve the variation of the displacement fields throughout the cycle. A time step of $\Delta t = 0.01$ s was used over a load period of 1 s, resulting in 100 increments. This discretization was found to give stable predictions of the crack growth direction.

Four-noded quadratic elements were used in the model, with mesh refinement in the crack area in order to accurately capture the near tip displacement field. A target element size of $h_c = 0.05$ mm was used in the crack tip region. The mesh is shown in Figure 3.5.

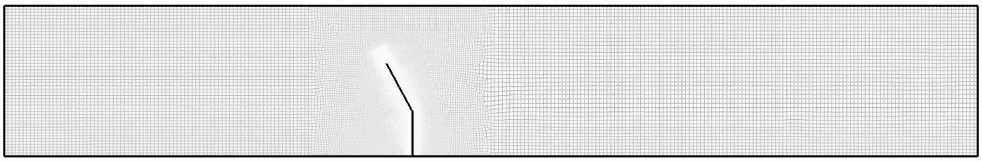

(a)

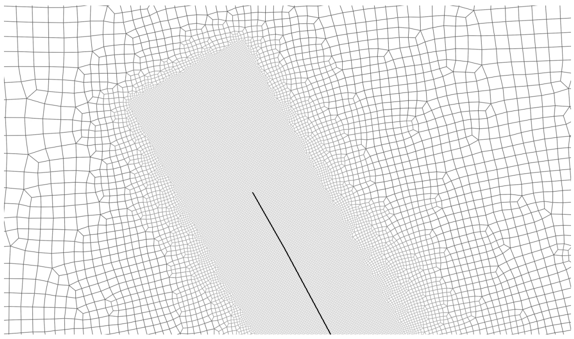

(b)

Figure 3.5: Mesh used for the FPB model. (a) Full model. (b) Refined mesh close to the crack tip.

The FE model without a crack was first validated against benchmark solutions, such as reaction forces and bending moment, in order to verify that the boundary conditions and load configuration correctly produce expected results for the setup.

3.1.2 Result and Discussion

The crack face displacements (δ_I, δ_{II}) were evaluated at a distance $d_h = 0.145$ mm from the crack tip. Predictions were first obtained at five instances along the experimentally observed crack path. The resulting crack growth directions and crack path are compared with the experiment in Figure 3.6.

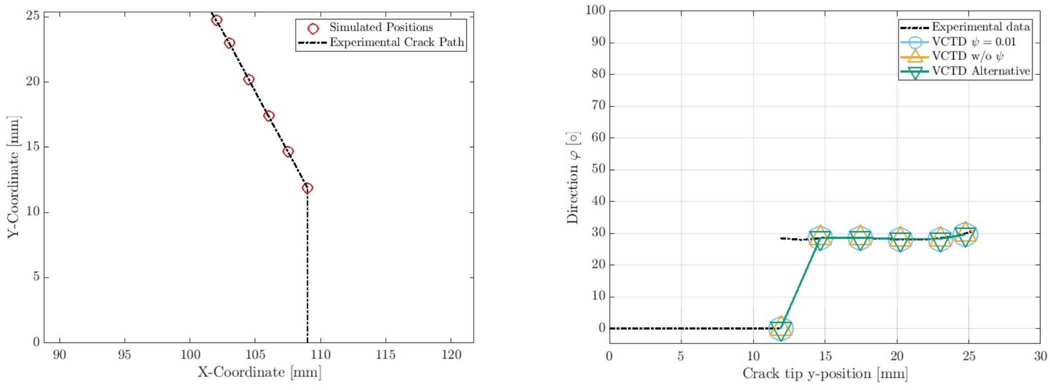

(a) **(b)**

Figure 3.6: FPB predictions evaluated along the experimentally observed crack path. (a) Crack path. (b) Crack growth direction.

All VCTD formulations give consistent predictions for most of the experimentally observed crack path. The largest discrepancy occurs at the first evaluated instance, where the crack transitions from the vertical pre-crack into the experimentally preferred fatigue crack direction. This part of the experiment is particularly sensitive, since it corresponds to the transition from the mode I pre-crack to the asymmetric four point bending load configuration. Although Qian and Fatemi [9] describe the general pre-cracking procedure, the local conditions governing the initial change in crack direction are not fully specified. The initial kink may therefore be influenced by effects such as residual stresses from pre-cracking, local microstructural variations, or small imperfections in the pre-crack geometry. These effects are not explicitly included in the present FE model, which may explain why none of the investigated VCTD formulations captures the initial kinking behavior.

After the initial kink, the crack path becomes considerably more stable. The crack has then aligned with a direction in which the mode II contribution is small, and the crack tip displacement response is dominated by opening. This is reflected in the ratio $\delta_I/|\delta_{II}| > 10$, indicating that the relative sliding displacement is small compared with the opening displacement. The accumulated VCTD vector is therefore controlled primarily by mode I deformation. As a result, the formulations that include or neglect reversed shear restrictions give practically identical predictions. The treatment of reversed shear becomes important only when sliding and crack face contact make a significant contribution to the load cycle evaluation, which is not the case for the FPB experiment after the initial reorientation.

Qian and Fatemi [9] correlated the crack growth rate using an effective stress intensity factor range originally proposed by Tanaka [23]. The corresponding Paris-type relation is written as

$$\frac{da}{dN} = 2.67 \times 10^{-13}(\Delta K_{eff})^{3.77}, \qquad \text{where} \quad \Delta K_{eff} = (\Delta K_I^4 + 8\Delta K_{II}^4)^{0.25}. \quad (3.1)$$

The estimated crack growth rates along the experimentally prescribed crack path are shown in Figure 3.7. The lower and upper estimates in Figure 3.7a were calculated using Equations (2.26) and (2.27) in Chapter 2, while the effective SIF estimate in Figure 3.7b was calculated using Equation (3.1).

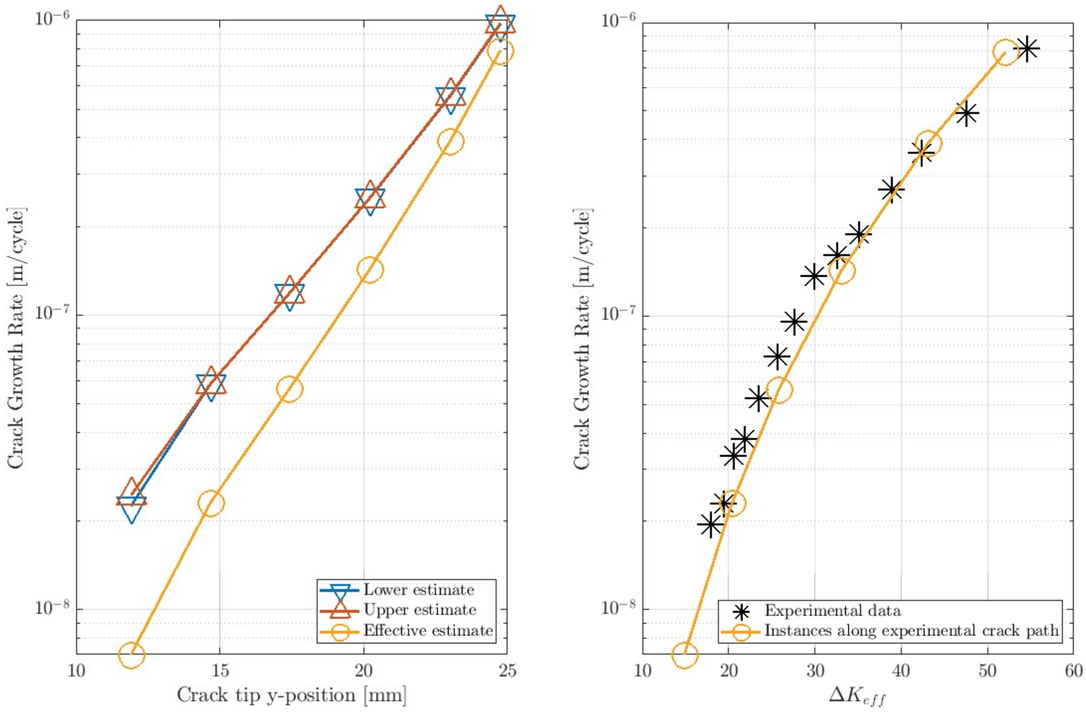

(a) **(b)**

Figure 3.7: FPB crack growth rate estimation for stationary points along experimental crack path. (a) Upper and lower crack growth rate estimate. (b) Crack growth rate based on Equation (3.1).

The lower and upper crack growth rate estimates are nearly identical after the first crack growth instance. This follows from the rapid decrease of $\Delta K_{II}/\Delta K_I$ as the crack propagates. Starting from the initial value $\Delta K_{II}/\Delta K_I = 0.262$, the ratio decreases to below 0.1 once the crack has kinked into its stable growth direction. The mode I range ΔK_I therefore dominates both rate expressions, and the mixed-mode interaction has only a minor influence on the predicted rate. The good agreement with the effective SIF correlation of Qian and Fatemi further supports the interpretation that the FPB crack becomes essentially mode I dominated after the initial kink.

A freely propagated crack path was then generated. Since the VCTD formulations did not reproduce the initial kink accurately, propagation was initiated from an already kinked crack configuration with crack length a = 3 mm. The predicted crack paths are compared with the experimental observations in Figure 3.8.

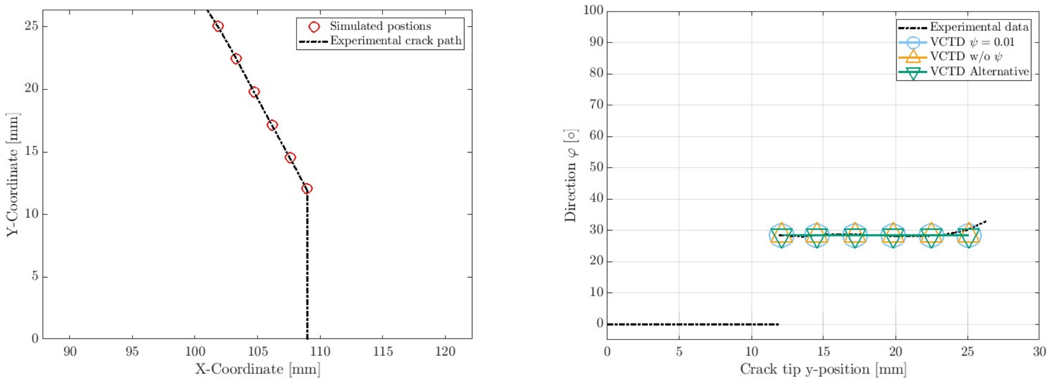

(a) **(b)**

Figure 3.8: FPB predictions by propagating the crack. (a) Crack path. (b) Crack growth direction.

The propagated path results further support the interpretation from the evaluation along the experimental crack path. All VCTD formulations produce nearly identical paths, and the predicted crack remains close to the experimentally observed straight inclined crack. This suggests that the main difficulty is associated with capturing the initial transition from the vertical pre-crack, rather than the subsequent crack propagation. Once the crack has kinked into the experimentally preferred direction, the mode I dominated loading promotes stable growth along the existing crack direction.

The crack growth rate estimates for the propagated path are shown in Figure 3.9.

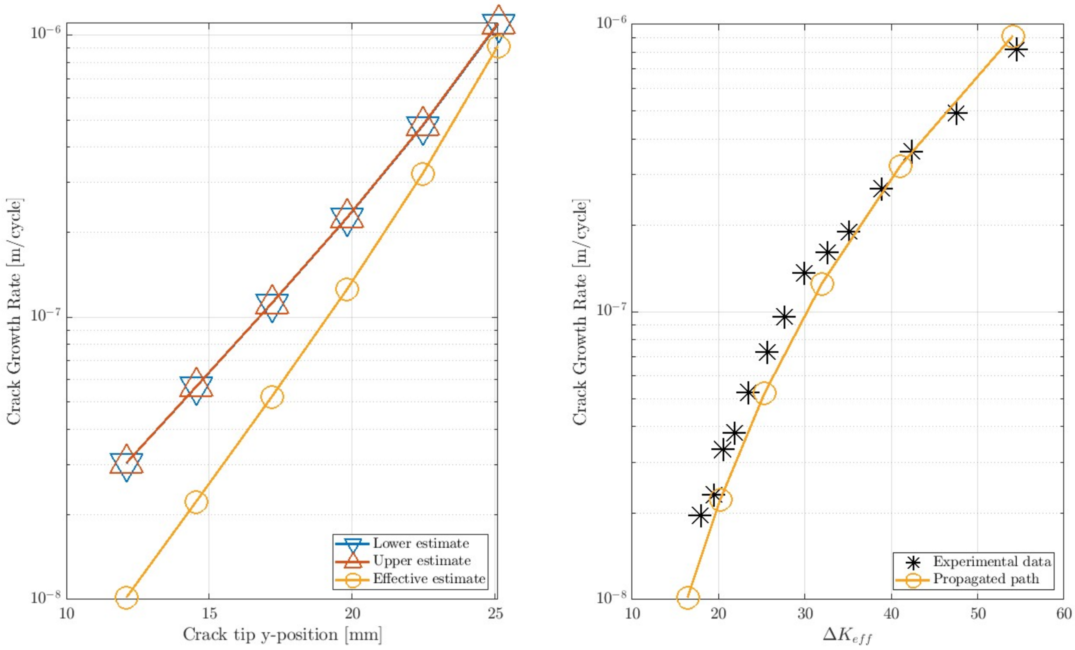

(a) **(b)**

Figure 3.9: FPB crack growth rate estimation for propagated crack. (a) Crack growth rate compared to stationary crack rates. (b) Crack growth rates for propagating and stationary points compared to experimental data, using Equation 3.1.

The propagated path gives crack growth rate estimates consistent with those obtained along the experimentally prescribed path. The ratio between the upper and lower estimates remains close together, $(da/dN)_{\text{upper}} / (da/dN)_{\text{lower}} < 1.01$, again demonstrating that the response is dominated by mode I. The close agreement between the lower and upper estimates should therefore not be interpreted as a general property of the employed rate equations, but as a consequence of the loading state in this particular experiment.

From the calculated rates of the freely propagated crack path, an estimated number of cycles to failure was calculated, shown in Figure 3.10 together with reported values from the litterature.

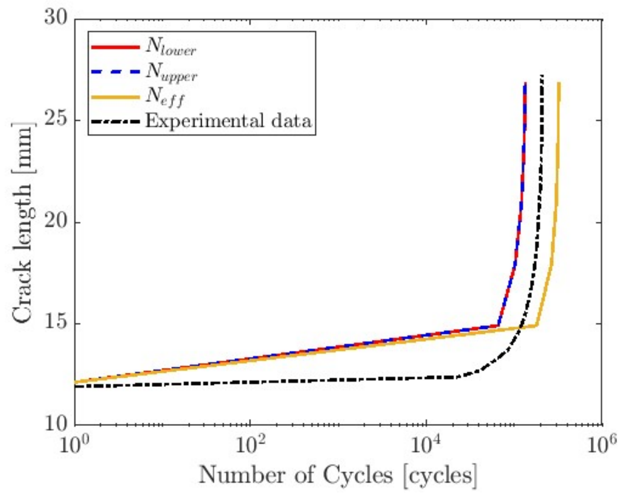

Figure 3.10: Estimated crack evaluation with cycles for the FPB experiment.

It can be seen that the estimated number of cycles for the upper and lower rate estimates are a bit conservative, but one should have in mind that the propagated path does not really start from the initial crack tip. Since the number of cycles needed for the crack to grow is a lot more in the beginning of the crack life, there is some cycles missing to reach the point of the first evaluation. However, using the rates based on the effective crack force ΔK_{eff} seen in Equation (3.1), the rate integration is a bit overestimated. The estimations together frames the reported experimental.

3.1.3 Sensitivity

Sensitivity studies were performed to quantify the influence of the numerical parameters used in the VCTD evaluation and SIF extraction. The purpose of these studies is to separate numerical uncertainty from modeling uncertainty. If the predicted directions are insensitive to numerical parameters such as time step, crack tip element size, and evaluation distance, remaining discrepancies are more likely related to the employed modeling assumptions of the model than to numerical resolution.

The time step (Δt) was investigated because the VCTD algorithm accumulates crack tip displacement information over one load cycle. A sufficiently small time step is required to resolve the variation of the displacement components, especially near the maximum load where the main contribution to the crack driving displacement occurs. The investigated time steps are summarized in Table 3.2.

Table 3.2: Time step sensitivity for the VCTD formulations of the FPB experiment.

Time step size	VCTD $\psi = 0.01$ φ [∘]	VCTD w/o ψ φ [∘]	Alternative VCTD φ [∘]
$\Delta t = 0.005$ s	6.66e-06	6.66e-06	-2.13e-06
$\Delta t = 0.010$ s, reference	-1.56e-05	-1.56e-05	-2.13e-06
$\Delta t = 0.050$ s	3.22e-06	3.22e-06	-2.13e-06

The investigated time step range produced only minor changes in the predicted crack growth direction, with the largest deviation below 1°. This confirms that $\Delta t = 0.01$ [s] is sufficiently small for the sinusoidal load used in the FPB simulations.

A mesh size sensitivity study was also carried out by varying the target element edge length (h_c) close to the crack tip. Accurate evaluation of the near tip displacement field is essential for the VCTD criterion, and the element size may therefore influence the predicted direction. The results are summarized in Table 3.3.

Table 3.3: Mesh size sensitivity for the VCTD formulations of the FPB experiment.

Element size near crack tip	VCTD $\psi = 0.01$ φ [∘]	VCTD w/o ψ φ [∘]	Alternative VCTD φ [∘]
$h_c = 0.03$ mm	-3.31e-06	-3.31e-06	-2.29e-06
$h_c = 0.05$ mm, reference	-1.56e-05	-1.56e-06	-2.13e-06
$h_c = 0.10$ mm	4.93e-05	4.93e-05	-5.45e-05

The mesh study showed only a small influence on the predicted crack growth direction, again, with the largest deviation below 1°. Which ensures that the chosen mesh size did not influence the results of the predicted crack growth direction.

The evaluation distance (d_h) was investigated separately. In analogy with the region of K-dominance for SIFs, the crack face displacement components (δ_I and δ_{II}) should be measured sufficiently close to the crack tip for the asymptotic crack tip field to dominate [17]. The sensitivity of the predicted direction to d_h is shown in Figure 3.11, showing only a minor effect on the predicted crack growth direction, with the largest deviation being $<<$ 1°.

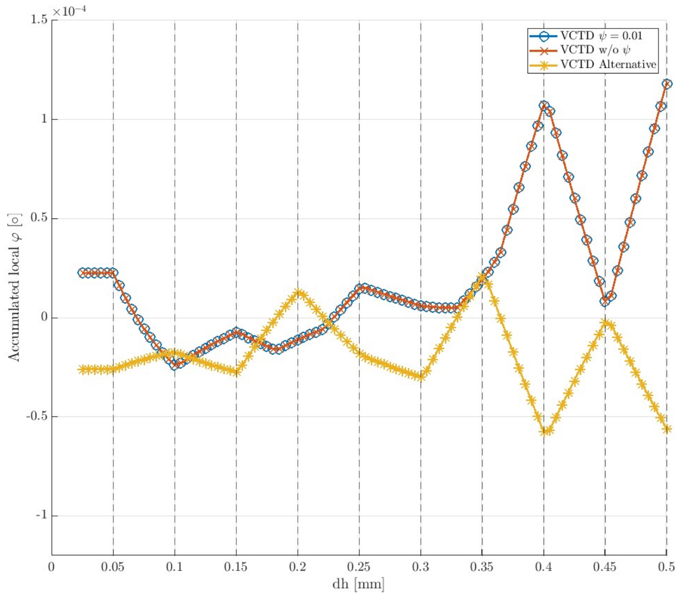

Figure 3.11: Sensitivity of evaluation point along crack faces on the predicted crack growth direction of the FPB experiment.

Lastly, SIF estimates are sensitive to the evaluation and contour choices. The ABAQUS contour used for extracting SIFs was therefore also examined. Five contours were extracted, where the first contour is closest to the crack tip and subsequent contours include progressively larger surrounding element rows. The resulting convergence of ΔK_I and ΔK_{II} in Figure 3.12 was shown to converge between the second and third contours, and contours from the third contour were therefore chosen and considered suitable for the crack growth rate estimates of the FPB experiment.

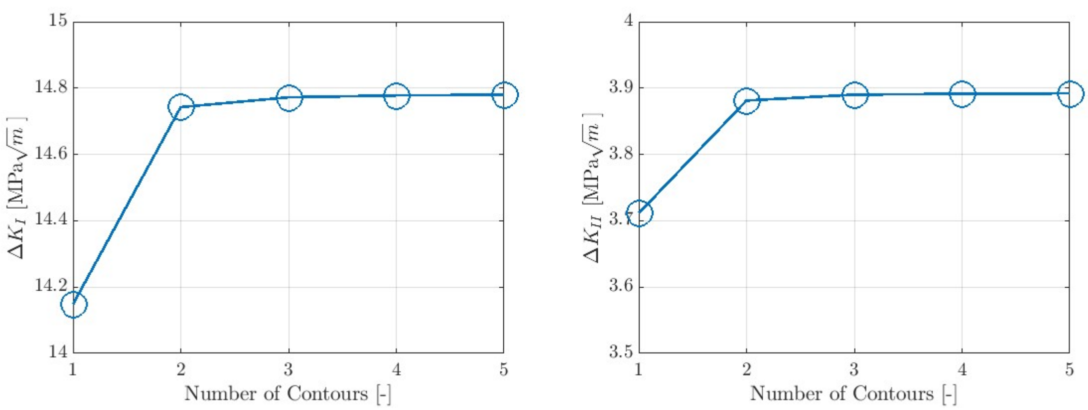

(a) **(b)**

Figure 3.12: Sensitivity of chosen contour in ABAQUS on obtained SIF ranges of the FPB experiment. (a) ΔK_I (b) ΔK_{II}

3.2 Compact Tension Shear

Fatigue crack behavior from notches under mixed mode loading was analyzed for the different formulations of VCTD criterion in terms of the Compact Tension Shear (CTS) specimen. The employed CTS experiment originally described by Ding et al. [24], and is illustrated in Figure 3.13. While the geometry and setup follow this work, the boundary conditions are adopted from Floros et al. [17]. It should be important to note that the boundary and loading conditions of the experiment may be enforced differently in order to emulate the physical cylindrical pins inside the holes of the specimen. However, minor differences between the setup does not affect the overall crack growth behavior.

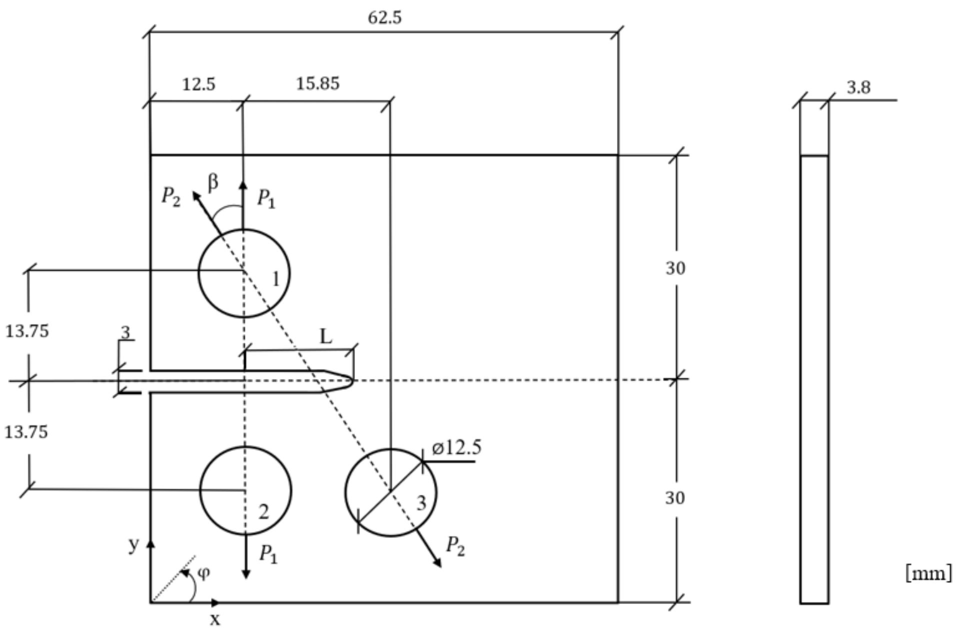

Figure 3.13: Dimensions and loading configurations in CTS experiment performed by Ding et al. [24]

(a)

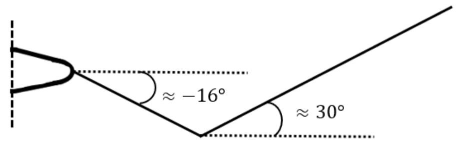

(b)

Figure 3.14: Crack initiation and propagation from the notch for the CTS experiment. (a) Detail of the notch. (b) Final crack configuration from notch.

The CTS specimen was initially pre-cracked under pure mode I loading, producing a crack inclined at φ ≈-16° with a length of 1.19 mm. It was subsequently subjected to a pulsating load applied in two loading configurations. In the first configuration, an uniform external load P_1 was applied in the y-direction in hole 1, whilst the displacements of all nodes in hole 2 were constrained in the y-direction, see Figure 3.13, this yielded to an experimental crack at an continued inclination of $\varphi \approx -16°$. This was followed by the second loading configuration, in which an external load P_2 was applied at hole 1 at an angle of $\beta = 30°$ relative to the y-axis, with displacements at hole 3 were constrained in both the x- and y-directions. This loading produced an experimental crack inclination of $\varphi \approx 30°$. The radius of the notch and the experimental crack path are illustrated in Figure 3.14. Having an incline crack w.r.t the loading direction and the change in loading direction modifies the stress state at the crack tip, introducing a combination of mode I and II deformation. As a result, the crack experiences mixed-mode loading, which influences the subsequent crack propagation direction. The two configurations are summarized in Table 3.4. Note that R-ratio is the ratio between the minimum force and maximum force, i.e., R $= \frac{F_{min}}{F_{max}}$. The specimen was made out of Q345R hot-rolled steel, where the Youngs's modulus and Poisson's ratio are, E = 212.5 GPa and $\nu = 0.29$, respectively [1].

Table 3.4: Test conditions according to Ding et al. [24] for the CTS experiment.

Load conf.	β [°]	φ [°]	$\Delta P/2$ [kN]	R-ratio [-]	r_0 [mm]	L [mm]
1	0	-16	2.25	0.1	0.5	10.859
2	30	30	3.15	0.1	0.5	10.859

3.2.1 FE setup

A two-dimensional FE model was constructed under linear elastic plane stress conditions due to the small thickness of the specimen. To prevent rigid body motion in the simulations, the lowest node of hole 2 was additionally constrained in the x-direction for both configurations. This constraint was furthermore introduced to better represent the experimental loading of the specimen using cylindrical pins.

In order to further replicate the experiment, a pulsating sinusoidal load was adopted using a time step of $\Delta t = 0.01$ s for each respective load configurations, these are shown in Figure 3.15.

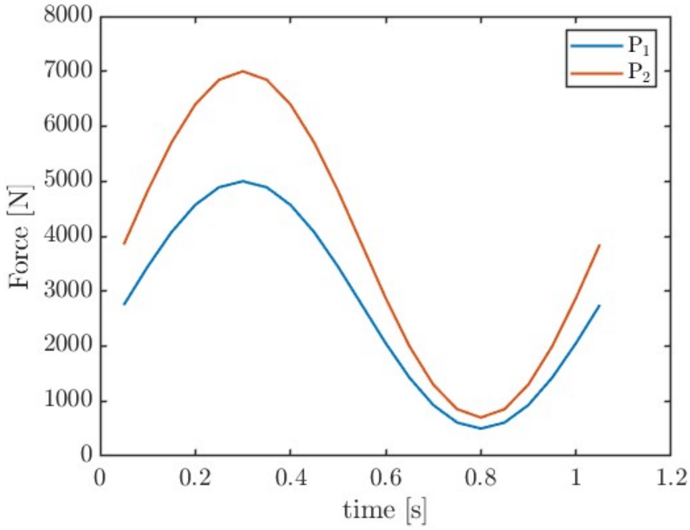

Figure 3.15: Load cycles for the two different load configurations for a timestep $\Delta t = 0.01$ s in CTS experiment.

The sinusoidal loads are offset from zero to represent a realistic pulsating load expected from a fatigue testing machine.

The mesh for the full specimen is shown in Figure 3.16a, where four-node quadrilateral elements were used throughout the entire model. To ensure sufficient accuracy in the regions of high stress concentration, the mesh was locally refined around the notch and crack tip, with a target element length of $h_c = 0.05$ mm. The resulting refined mesh in these critical regions is shown in Figure 3.16b.

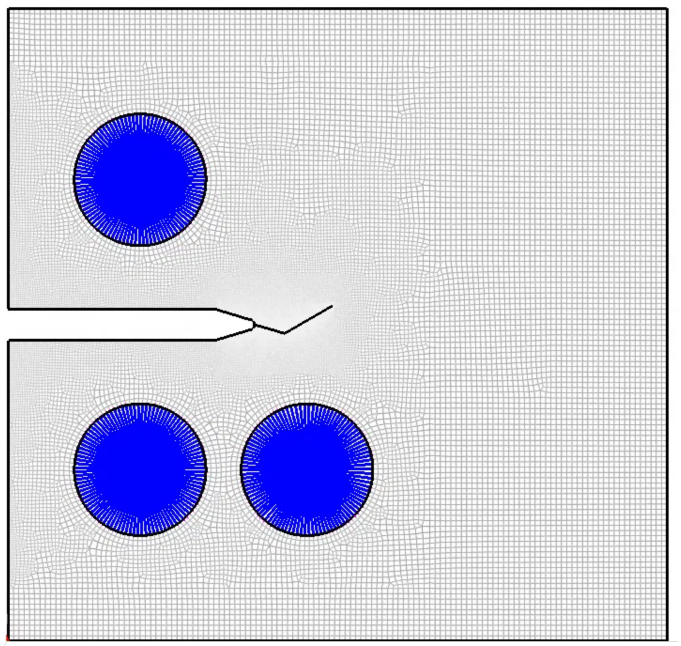

(a)

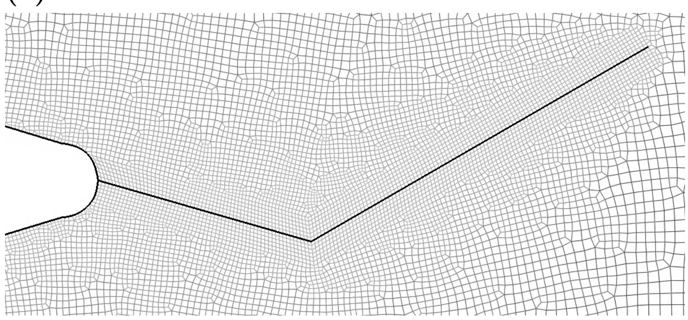

(b)

Figure 3.16: FE mesh for the CTS experiment. (a) Mesh of full model. (b) Mesh zoomed in at notch area and around the crack tip

3.2.2 Result and Discussion

The prediction of crack growth direction was first investigated for a stationary crack. Seven isolated positions on the crack are analyzed, corresponding to different points along both the initial and fully developed cracks. For the initial crack branch, the positions selected are 50%, 75%, and 0.05 mm from the full initial crack length, and the full initial crack length itself. Furthermore, for the second crack branch, 25%, 75%, and the full crack length were considered. The evaluation for the stationary crack serve as discrete points along the experimental crack path, providing reference positions to verify whether the crack follows the experimental path.

The crack growth direction was evaluated at a distance $d_h = 0.175$ mm from the crack tip. Following the experimental crack path using stationary crack instances, the corresponding stationary points were evaluated. These isolated points of evaluation are shown in Figure 3.17a, whilst the resulting direction predicted by the VCTD criteria are shown in along the crack are illustrated by Figure 3.17b.

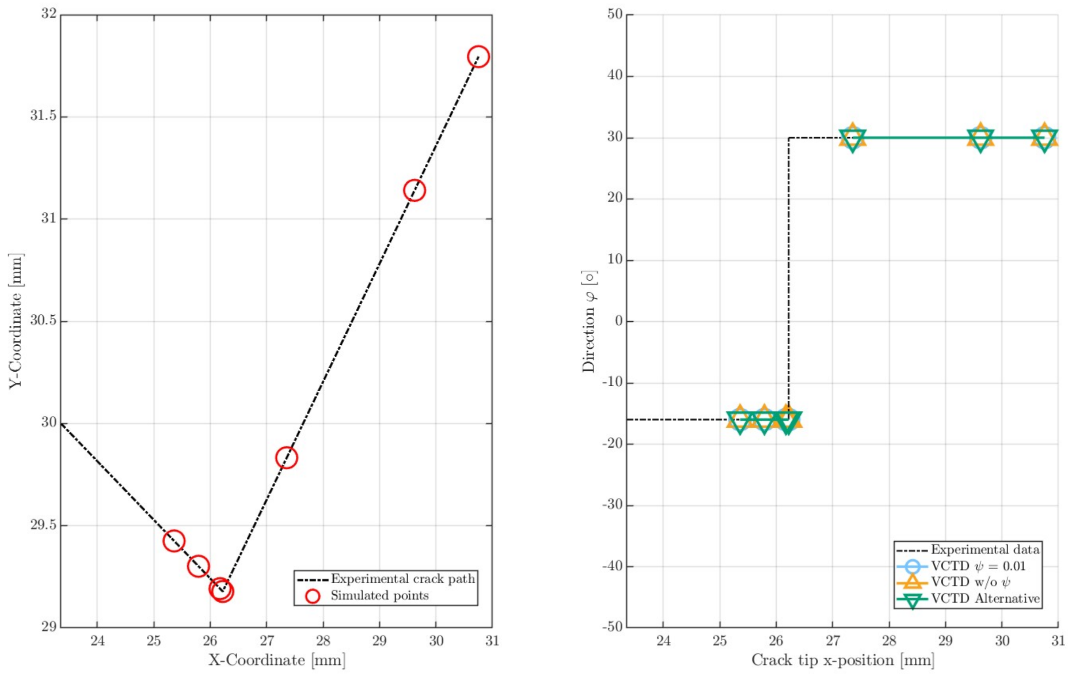

(a) **(b)**

Figure 3.17: Stationary points along the experminetal crack path in the CTS experiment. (a) Stationary points along the experimental path. (b) The resulting predicted crack growth direction.

Upon evaluating the crack growth direction at isolated points along the crack path, it is evident that the predicted directions align well with the experimental trajectory, as shown in Figure 3.17b. Furthermore, comparison of the crack growth directions predicted by the various VCTD criteria indicates consistent predictive accuracy throughout different evaluation points, as no deviation from the criteria was produced.

One possible explanation for this behavior is the mode I dominated mixed-mode loading condition. This is evident from the consistently open crack during propagation due to the tensile loading, indicating a relatively minor contribution from shear loading. The crack tip displacement ratio, $\delta_I/\delta_{II} > 50$, further confirms that the opening displacement dominates over the sliding displacement at the crack tip. Evaluating the reverse shear condition in Equation (2.9) shows that the ratio $\delta_I/|\delta_{II}|$ remains significantly greater than the selected parameter $\psi = 0.01$ throughout crack propagation. This indicates that the reverse shear restriction remains inactive, causing the VCTD formulations with and without reverse shear to become effectively identical for the present loading case, thereby explaining the coinciding crack growth predictions. A similar equivalence is observed for the alternative formulation based on the crack driving displacement vector, given in Equation (2.19). Since δ_I remains significantly larger than δ_{II}, the mode I displacement continues to dominate in the accumulation scheme of the crack growth direction, resulting in almost identical predictions.

Overall, because the predicted stationary crack growth directions follow the experimental crack path closely, it can be claimed that the investigated VCTD criteria are capable capturing straight crack paths under mode I dominated mixed-mode loading.

Assessing the crack growth rate experimentally observed data given by Ding et al. [24] with the simulated stationary points using the upper and lower bounds given by Equations 2.26 and 2.27, and using the Paris law constants C = $1.49{\times}10^{-9}\ \frac{mm/cycle}{MPa\sqrt{m}}$ and m = 3.41 for material Q345R [25], yields the following results presented in Figure 3.18.

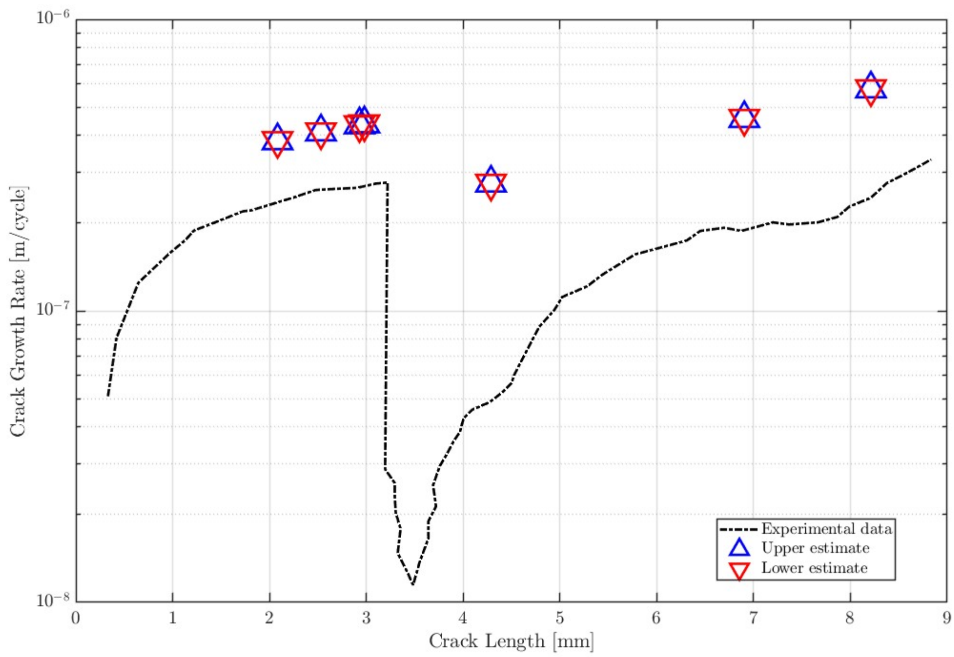

Figure 3.18: Crack growth rate for upper and lower bounds for stationary points in the CTS experiment.

A comparison between the experimental data reported by Ding et al. [24] for the CTS specimen and the resulting crack growth rates for the upper and lower bound predictions obtained from ABAQUS is illustrated in Figure 3.18. It can be seen that the results produced by ABAQUS are of the same order of magnitude as the experimental results. Furthermore, these predictions follow the overall trend observed in the experimental data. It should be noted that the upper and lower bound crack growth rate predictions overlap almost completely, with a relative difference of less than 0.1% at each evaluation point. This indicates that the influence of ΔK_{II} on the predicted crack growth rates is negligible compared to that of ΔK_{I}, which is consistent with mode I dominated loading. However, both estimates consistently overestimate the experimentally measured crack growth rate.

The consistent overprediction of the crack growth rate is most likely associated with the modeling assumptions employed in the numerical framework. In particular, the method used to evaluate the SIFs may not fully capture the crack tip fields under the present mixed-mode conditions. Furthermore, the equivalent SIFs formulation used to represent the combined mode I and mode II loading may not be entirely representative of the experimental crack growth behavior. Since the crack growth rate prediction is directly governed by the evaluated crack driving force, the equivalent SIFs formulation made by ABAQUS can significantly influence the predicted growth rates.

Additionally, the FE model does not account for material microstructural effects, which may contribute to discrepancies compared to the experimentally observed behavior. Furthermore, the stationary crack assumption evaluates the crack growth response at isolated crack configurations and may therefore not fully capture the continuous evolution of crack propagation observed experimentally.

Subsequently, the predicted crack growth direction was analyzed considering growth lengths of l = 0.5 mm, with 3–6 evaluation points assigned to each branch of the crack.

Numerical predictions were also obtained by propagating the crack from the initial crack position, where the predicted crack growth direction was analyzed considering growth lengths of l = 0.5 mm. Figure 3.19a shows the protected crack growth direction given by the resulting positions in Figure 3.48b.

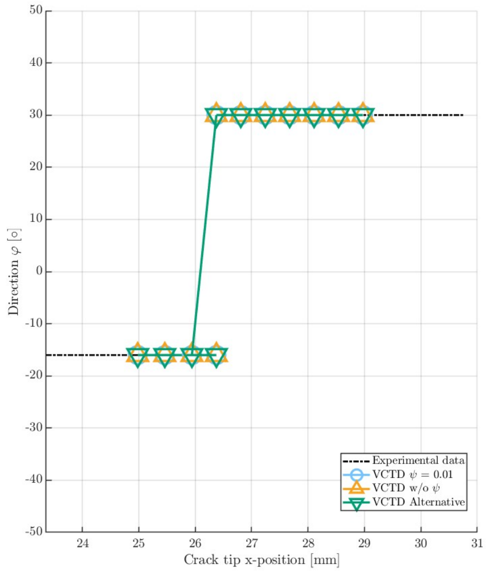

(a)

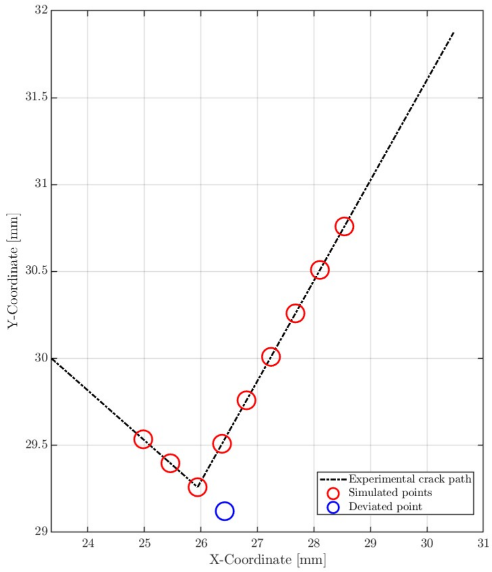

(b)

Figure 3.19: Propagating points for the CTS experiment. (a) Predictive crack growth directions obtained by propagation. (b) Resulting positions along the crack from propagation for the different VCTD criterion.

As shown in Figure 3.19, the propagated crack positions generally follow the experimentally observed crack path, further confirming that all VCTD formulations are capable of predicting crack growth direction accurately for predominantly straight crack propagation. Furthermore, all three formulations produce almost identical predictive coordinates, as shown by Figure 3.19a, given the predictive crack growth direction throughout the analysis. However, the criteria collectively fail to capture the abrupt change in crack growth direction associated with the change in loading configuration, as evidenced by the blue deviating propagated position near the end of the first crack branch, clearly illustrated in Figure 3.19b. Consequently, a manual kink was introduced to reproduce the sharp transition in the crack path, as evident by the first point of the second crack branch, and the subsequent points after the fact. The manually introduced kink was not intended as a validation of crack path prediction, but rather as a means of investigating the post-kink crack growth response once the experimentally observed branch had formed.

Several factors may contribute to why the kinking was not captured. Simplifications inherent to the FE framework may influence the crack tip displacement fields, for example, the microstructural features present in the experiment which can not be replicated in the FE simulation, can therefore affect the predicted crack growth direction. In addition, uncertainties associated with the experimental crack path measurements and the absence of reported loading changed between the two loading configurations in the reference study may also contribute to differences between the numerical and experimental paths.

Finally, the results may suggest a limitation of the VCTD criterion itself in capturing abrupt directional changes. Since the criterion is based on accumulated crack tip displacement components along the existing propagation path, it may be inherently better suited to straight or gradually curving crack propagation rather than sudden kinking behavior.

The crack growth rates obtained from the propagating crack positions are presented as upper and lower bound estimates using the same Paris law constants introduced previously for the stationary investigations. The manually introduced kinking point was excluded from comparison of crack growth rates. The resulting predictions are shown in Figure 3.20

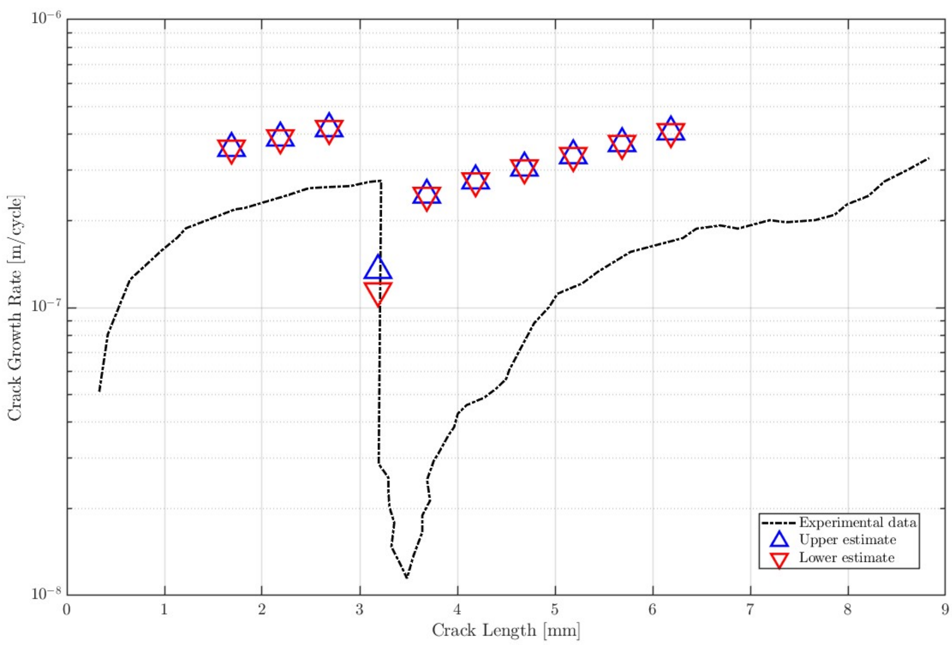

Figure 3.20: Crack growth rate for upper and lower bounds for propagating points in the CTS experiment.

Illustrated by Figure 3.20, the upper and lower bounds shows an overestimation of the experimentally measured crack growth rate, which once again can be attributed to the simplification of the FE model. An important observation from the comparison between the stationary and propagating points is that the estimates obtained from the propagating points show better agreement with the experimental values. The improved estimation obtained from propagated crack positions suggests that continuous crack propagation better captures the evolving crack tip stress field and loading history compared to isolated stationary evaluations. This indicates that crack growth rate prediction is sensitive not only to the local crack geometry, but also to the progressive redistribution of stresses during crack extension.

Although the propagating crack growth direction analysis did not capture the abrupt crack kinking observed experimentally, the crack growth rate response still captures a significant transition at the corresponding propagation point, evidenced by the pronounced reduction in crack growth rate associated with the change in loading configuration.

Furthermore, at the kinking transition point, the upper and lower bounds diverge with a separation of approximately 43%, reflecting the introduction of a more significant ΔK_{II} contribution associated with the change in loading configuration, however, at the next propagating position, the difference between upper and lower bounds are not as pronounced, implying that the crack propagation returns to a more mode I dominating loading. It should be noted that there is no fatigue number of cycles until failure reported in the experiment [24], therefore, the fatigue life calculations is not preformed.

3.2.3 Sensitivity

In order to evaluate the robustness of the CTS experiment, different parameters have been subjected to sensitivity studies. The outcomes of these sensitivities are the motivation to why certain parameters are used in the crack growth direction and rates evaluations.

The distance from the crack tip (d_h) has been evaluated with respect to the accumulated local crack growth direction given by the formulations of the VCTD, this is illustrated in Figure 3.21.

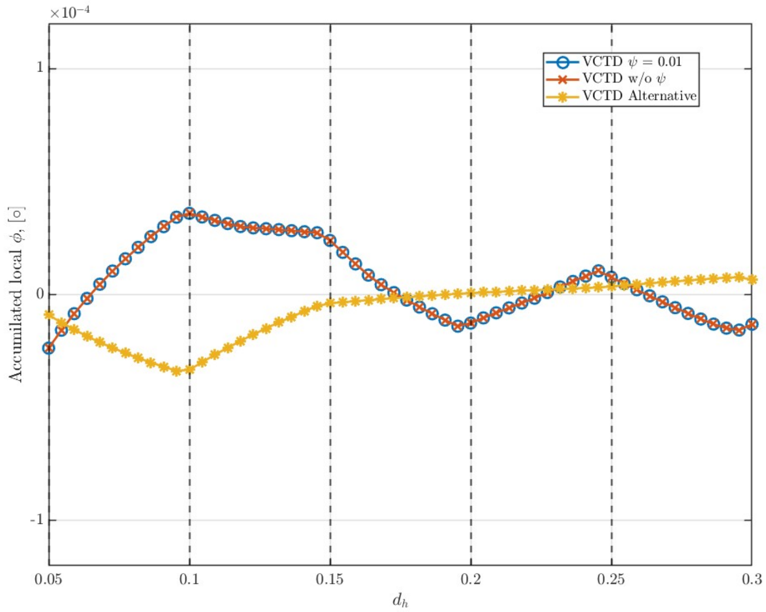

Figure 3.21: d_h sensitivity compared to the accumulated crack growth direction for the CTS experiment.

The results from this study showed a minor effect in the predicted crack growth direction, as the largest deviation is much smaller than 1°. However, a d_h should not be too close or to far from the crack, which is why a chosen d_h parameter between 0.15 mm and 0.25 mm are an optimal choice.

An analysis of the influence of the time step size (Δt), and the crack tip mesh size (h_c) from the initial crack was conducted for the various VCTD formulations, as presented in Tables 3.6 and 3.5, respectively. Three different time step sizes, $\Delta t = 0.05$, 0.01, and 0.001 s together with three crack tip mesh sizes, $h_c = 0.1$, 0.05, and 0.03 mm were investigated.

Table 3.5: Mesh size sensitivity for the VCTD formulations for the CTS experiment.

Element size near crack tip [mm]	VCTD $\psi = 0.01$ φ [∘]	VCTD w/o ψ φ [∘]	Alt. VCTD φ [∘]
$h_c = 0.03$	1.38e-06	1.38e-06	1.41e-06
$h_c = 0.05$	-1.72-06	-1.72e-06	8.0e-06
$h_c = 0.10$	1.38e-06	1.38e-06	-1.24e-5

The mesh sensitivity analysis presented in Table 3.5 indicates that the crack growth direction predictions exhibit only limited sensitivity to the crack tip mesh size. The largest variation in the accumulated crack growth angle was observed between the coarsest and finest meshes, $h_c = 0.1$ and 0.03, respectively. However, the differences between the meshes $h_c = 0.05$ and 0.03 were comparatively small, suggesting that the predictions were sufficiently converged for the chosen mesh size of $h_c = 0.05$ mm.

Table 3.6: Time step sensitivity for the VCTD formulations for the CTS experiment.

Time step size	VCTD $\psi = 0.01$ φ [∘]	VCTD w/o ψ φ [∘]	Alternative VCTD φ [∘]
$\Delta t = 0.005$ s	8.7e-07	8.7e-07	1.39e-06
$\Delta t = 0.010$ s	8.0e-07	8.0e-07	1.38e-06
$\Delta t = 0.050$ s	-2.308e-05	-2.31e-05	3.07e-05

As shown in Table 3.6, the predicted crack growth angle exhibits decreasing sensitivity with progressive refinement of the time step. The results obtained for $\Delta t = 0.01$ were therefore considered sufficiently stable, since additional reduction of the time step resulted in only marginal changes to the accumulated crack growth angle.

SIF evaluation is performed using to five contours in ABAQUS. Thus, to evaluate which contour is sufficient for crack growth rate analysis, a convergence analysis was performed, where the contours where compared to their resulting ΔK_I and ΔK_{II}, the resulting convergence is shown in Figure 3.22.

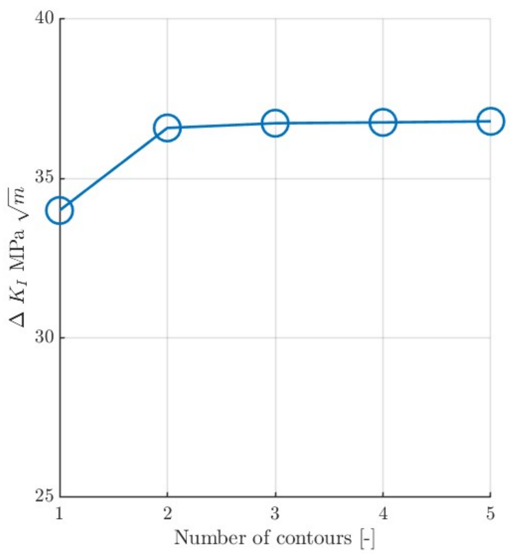

(a)

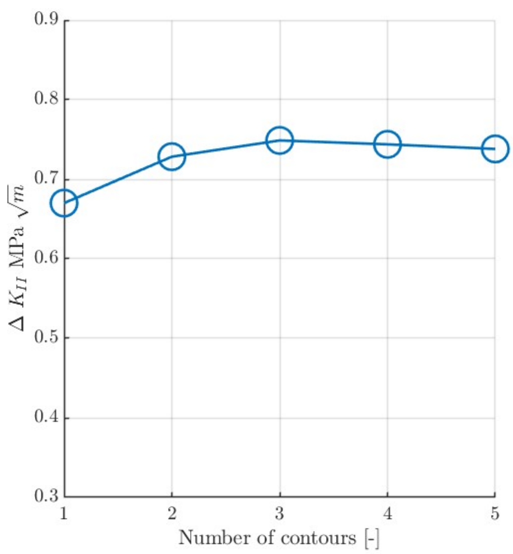

(b)

Figure 3.22: Sensitivity of chosen contour in ABAQUS on obtained SIF ranges of the CTS experiment. (a) ΔK_I (b) ΔK_{II}

From the convergence study, it is clear that ΔK_I converges after the second contour, whilst ΔK_{II} converges after the third contour. However, due to the fact that ΔK_I

has more influence in the crack growth rate, it is important to chose a contour number which is representative of the stress field. It is for this reason that contour 4 was chosen to be sufficient for the SIF analysis.

Furthermore, a study on the mesh structure was conducted to compare the refinement zone around the crack tip for the initial branch of the crack. The analysis compared radial and rectangular refinement strategies for the CTS specimen, focusing on their effect on the resulting crack growth rates. The effect of the mesh structure was quantified by evaluating the ratio of crack growth rates between the radial and rectangular refinement zones for both the upper and lower bounds. These ratios were computed across contour number 4 in ABAQUS, providing a systematic comparison of the mesh influence on the crack growth response.

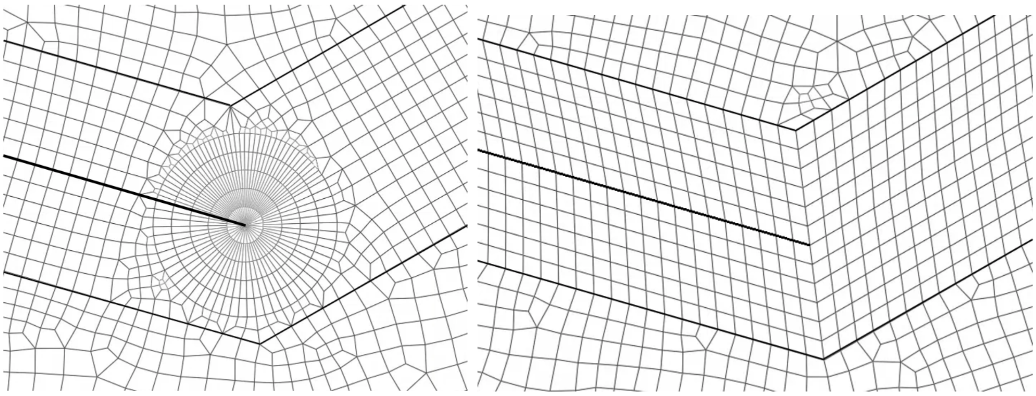

(a) **(b)**

Figure 3.23: Mesh structure comparison for the CTS experiment. (a) Radial mesh at the crack tip for the initial crack branch. (b) Rectangular mesh at the crack tip for the initial crack branch

The effect of the mesh structure was done by evaluating the ratio of crack growth rates between the radial and rectangular refinement zones for both the upper and lower bounds, computed across contour number 4 in ABAQUS. This yielded values of 1.43 for both the upper and lower bounds respectively, indicating that the choice of refinement strategy differentiate with approximately 43% in the predicted crack growth rates. The rectangular refinement zone was adopted for the presented analyses in this section based on the fact that rectangular refinement zones produced better conditioned elements near the crack tip, furthermore, the crack grows predominantly in one direction, which indicated that the rectangular zone aligned with that direction may better capture the stress field ahead of the tip. Additionally, rectangular refinement zones were adopted in the presented analyses due to their simpler mesh generation procedure compared to the radial refinement approach.

3.3 Biaxial Stress

This section considers two biaxial stress experiments in rail grade steel, designated as "RSB8" and "RSB3" by Bold [26]. These experiments are particularly relevant because they involve shear-dominated fatigue crack growth in rail grade steel, which is difficult to reproduce under conventional proportional mixed-mode loading. The experiments were performed on cruciform specimens with a central spark eroded notch, as shown in Figure 3.24. A 4 mm spark-eroded notch was introduced at an angle of 45° and subsequently pre-cracked under mode I loading to a total crack length of 5.7 mm, measured from crack tip to crack tip..

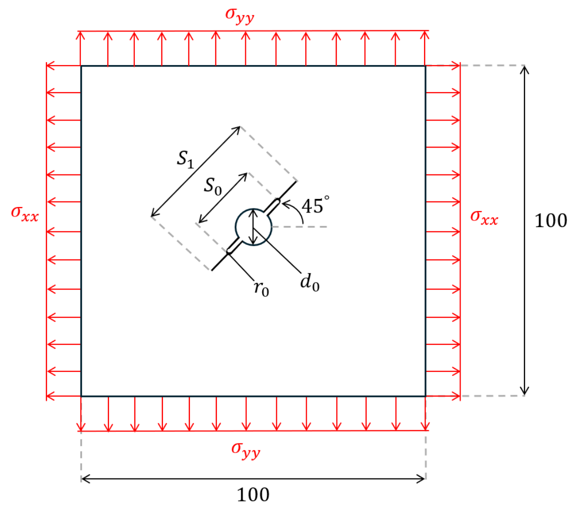

Figure 3.24: Biaxial stress experimental setup in Bold [26].

The two experiments differ in the applied load sequence. "RSB8" was subjected to sequential non-proportional loading, consisting of a pulsating mode I cycle followed by a fully reversed mode II cycle with respect to the initial 45° crack, see Figure 3.25a. "RSB3" was subjected to fully reversed mode II loading superimposed on a static mode I loading, as shown in Figure 3.25b.

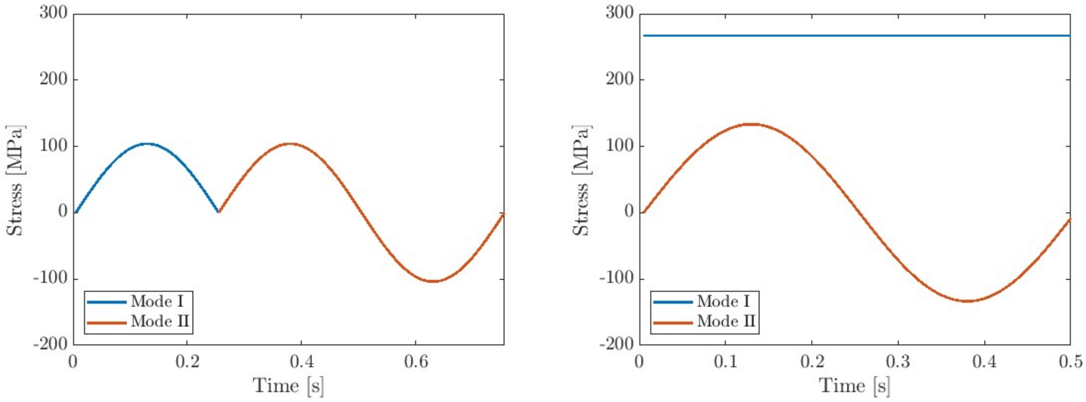

(a) **(b)**

Figure 3.25: Load configurations for the biaxial stress experiments in Bold [26]. (a) "RSB8" Experiment: Stable shear-mode crack growth. (b) "RSB3" Experiment: Shear-mode crack growth followed by mode I crack kinking.

For a crack inclined at 45° in a cruciform specimen, a tensile stress field applied equally in the x- and y-directions produces pure mode I opening of the crack, whereas tension in one direction and compression in the other produces mode II shear on the crack plane [26]. The RSB8 load sequence resulted in stable coplanar growth along the original crack plane. In contrast, RSB3 initially produced shear-mode growth, followed by kinking into a tensile-mode-dominated branch. The experimentally observed crack paths are shown in Figure 3.26.

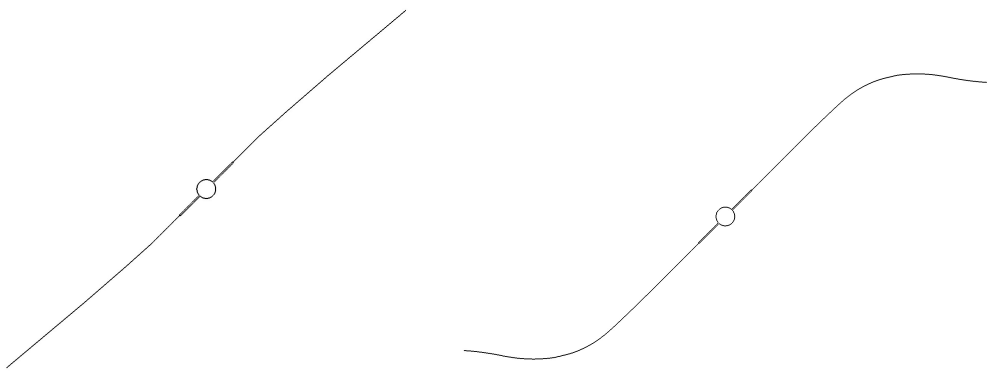

(a) **(b)**

Figure 3.26: Obtained crack paths for the biaxial stress experiments in Bold [26]. (a) "RSB8" Experiment: Stable shear-mode crack growth. (b) "RSB3" Experiment: Shear-mode crack growth followed by crack kinking.

During the propagation, the local crack path direction (φ) is defined by the counter-clockwise direction from the x-axis. From Bold [26], the specimen was taken to represent a standard rail grade steel, here modeled with elastic properties following the R260 material assumption used by Floros et al. [17]. The experimental conditions are summarized in Table 3.7.

Table 3.7: Test conditions for the biaxial stress experiments used by Bold [26]

r_0	d_0	S_0	S_1	RSB8		RSB3	
				ΔMode I	ΔMode II	Mode I	ΔMode II
[mm]	[mm]	[mm]	[mm]	[MPa]	[MPa]	[MPa]	[MPa]
0.3	1.0	4	5.7	104	208	267	267

3.3.1 FE setup

The biaxial stress experiments were modeled using linear elastic plane stress simulations. The FE setup is shown in Figure 3.27.

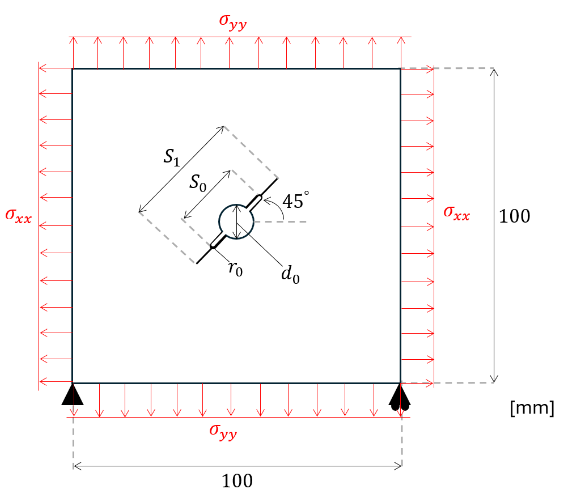

Figure 3.27: Visualization of biaxial stress experiments FE setup.

The experimental mode I and mode II stress components were applied through remote stress fields (σ_{xx} and σ_{yy}). The relation between the global stress components and the normal and shear stresses on a plane inclined by an angle (θ) follows from the plane stress transformation equations [1],

$$\sigma = \frac{\sigma_{xx} + \sigma_{yy}}{2} + \frac{\sigma_{xx} - \sigma_{yy}}{2}\cos(2\theta) + \tau_{xy}\sin(2\theta) \tag{3.2}$$
$$\implies \sigma = \sigma_{xx}\cos^2(\theta) + \sigma_{yy}\sin^2(\theta) + 2\tau_{xy}\sin(\theta)\cos(\theta)$$

$$\tau = \frac{\sigma_{yy} - \sigma_{xx}}{2}\sin(\theta) + \tau_{xy}\cos(2\theta) \tag{3.3}$$
$$\implies \tau = (\sigma_{yy} - \sigma_{xx})\sin(\theta)\cos(\theta) + \tau_{xy}(\cos^2(\theta) - \sin^2(\theta)).$$

For the present crack orientation, $\theta = 45°$ and no remote shear stress was applied, i.e, $\tau_{xy} = 0$. Thus, equal biaxial tension gives pure normal loading on the crack plane, while equal-magnitude tension/compression in the two global directions gives pure shear loading on the crack plane:

$$\begin{aligned} \sigma_{xx} = \sigma_{yy} &= \sigma & \text{mode I loading,} \\ -\sigma_{xx} = \sigma_{yy} &= \tau & \text{mode II loading.} \end{aligned}$$

The resulting applied load to the FE model are shown in Figure 3.28.

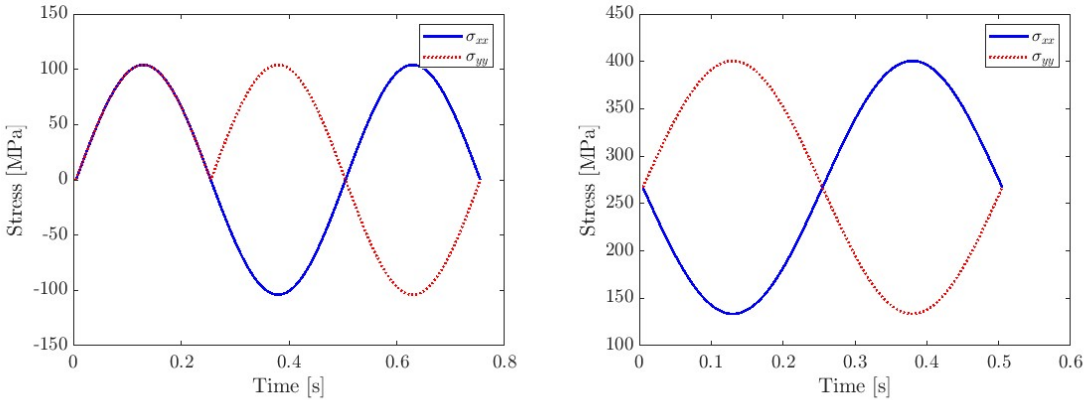

(a) **(b)**

Figure 3.28: Load cycles of the two biaxial stress experiments in FE simulations. (a) "RSB8" Experiment: Stable shear-mode crack growth. (b) "RSB3" Experiment: Shear-mode crack growth followed by mode I crack kinking.

A time step of $\Delta t = 0.005$ s was used for both experiments. For "RSB8", the simulated load period was 0.75 s, while for "RSB3" it was 0.50 s. The chosen time step was found to give stable crack growth direction predictions, as presented in the sensitivity study. It can also be noticed that the part of the loading in "RSB8" experiment, with the pure mode II loading, will experience contact between the crack faces. This was modeled using the general penalty method in ABAQUS, as presented in Section 2.4.

The mesh was refined near the crack tip using a target element size of $h_c = 0.05$ mm. The mesh used for "RSB3" is shown in Figure 3.29; the same crack tip refinement strategy was used for "RSB8".

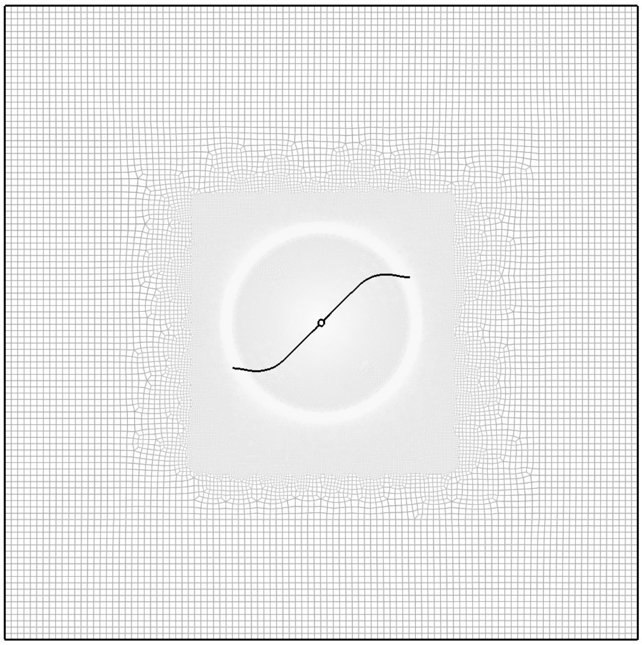

(a)

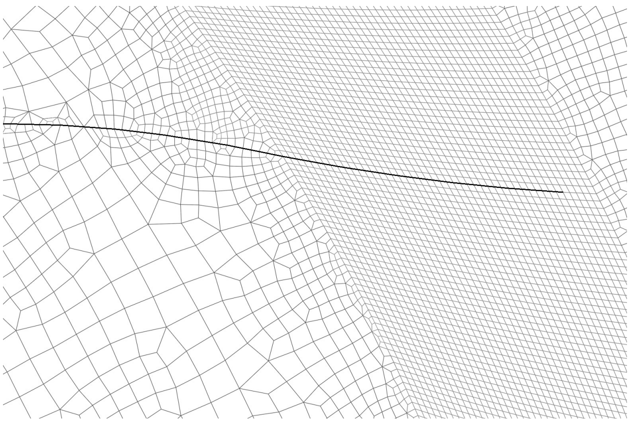

(b)

Figure 3.29: FE mesh used for the "RSB3" model. (a) Full model. (b) Refined mesh close to the crack tip.

The two cracks were assumed to grow symmetrically from the notch, in accordance with the experimental description by Bold [26]. This assumption reduces the numerical problem while preserving the main crack tip loading mechanism for the investigated symmetric load cases.

3.3.2 RSB8

The RSB8 experiment is used as a validation case for stable shear-mode crack growth under non-proportional loading. The load sequence consists of a pulsating mode I cycle followed by a fully reversed mode II cycle with respect to the initial 45° crack, see Figure 3.25a The mode I part of the cycle opens the crack, while the subsequent mode II part produces the sliding displacement responsible for coplanar shear-mode growth. Bold showed that this type of sequential loading can produce extensive coplanar growth in rail grade steel, in contrast to many pure or proportional mode II fatigue tests where the crack arrests or branches into mode I growth [26].

3.3.2.1 Results and Discussion

The crack face displacements (δ_I, δ_{II}) were evaluated at a distance $d_h = 0.145$ mm from the crack tip. Predictions were obtained at six instances along the experimentally observed "RSB8" crack path, shown in Figure 3.26a, and the results are presented in Figure 3.30.

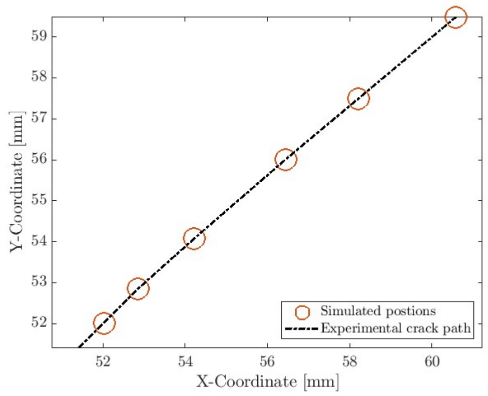

(a)

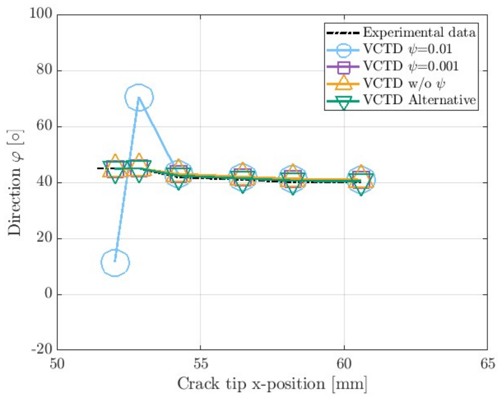

(b)

Figure 3.30: "RSB8" predictions evaluated along the experimentally observed crack path. (a) Crack path. (b) Crack growth direction.

The instance evaluation following the experimental path shows the formulation without the reversed shear threshold and the alternative VCTD formulation give stable predictions close to the experimentally observed coplanar path. However, the VCTD criterion can reproduce the experimentally observed coplanar crack growth when reversed shear contributions are not filtered too restrictively. The crack remains close to the original crack plane, indicating that the fatigue process is primarily governed by accumulated cyclic sliding at the crack tip rather than by tensile opening alone.

The formulation employing the reversed shear threshold $\psi = 0.01$ is the clear exception, giving poor predictions at the first two evaluated instances. This discrepancy is related to the treatment of reversed shear when the crack is nearly closed. During the fully reversed mode II part of the sequence, the crack faces slide relative to each other while the opening displacement may be small or zero. The ratio $\delta_I/|\delta_{II}|$, which controls whether reversed shear is included, can therefore become highly sensitive to small numerical changes in δ_I. The poor initial prediction should therefore be interpreted as a sensitivity of the reversed shear filtering condition, rather than as a failure of the displacement-based VCTD concept itself.

When reversed shear is neglected, the prediction becomes consistent with the observed shear-mode path. The formulation with $\psi = 0.001$ also performs well for the reference mesh, but the mesh sensitivity study later in this section shows that this result is less robust and the threshold based reversed shear filtering must be used with care.

The upper and lower crack growth rate estimates for the six instances along the experimental path are shown in Figure 3.31. The material parameters used to estimate the rate were taken for a general ferritic-pearlitic steel as $C = 6.89 \times 10^{-9} \frac{\mathrm{mm/cycle}}{(\mathrm{MPa}\sqrt{\mathrm{m}})^{\mathrm{m}}}$ and $m = 3.0$, according to Dowling [1]. These were used since no experimental values was reported. The rates are also compared with the experimental rates experienced and reported by Bold [26].

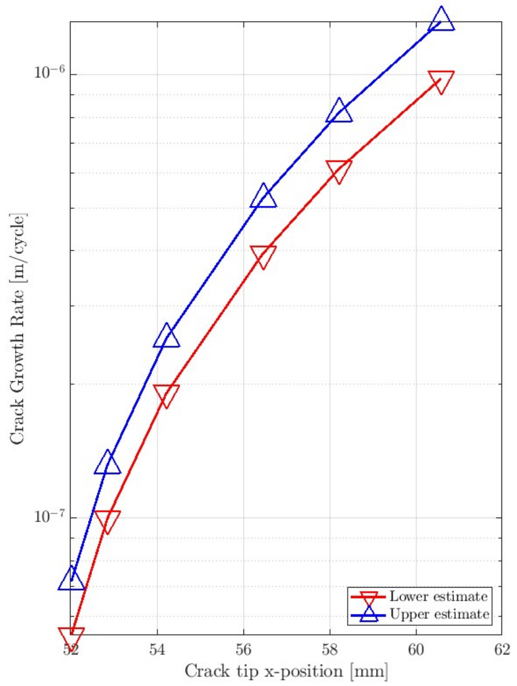

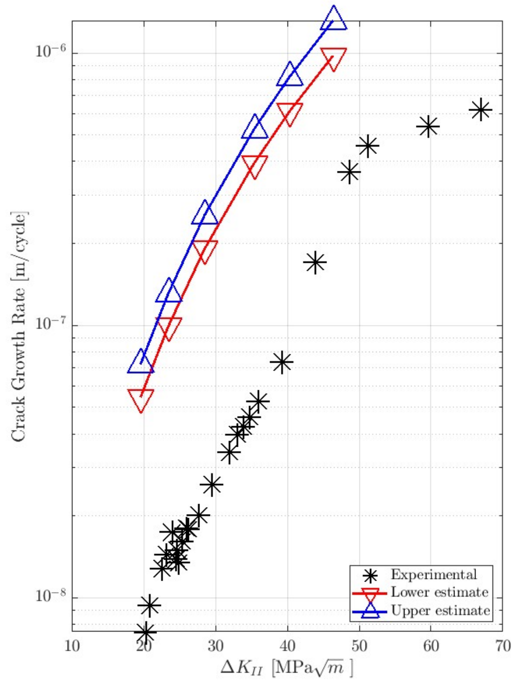

(a) **(b)**

Figure 3.31: "RSB8" crack growth rate estimates along the experimentally prescribed path. (a) Lower and upper estimates. (b) Rate plotted against ΔK_{II}.

Both the upper and lower estimates overpredict the experimentally reported crack growth rates. The predictions are therefore conservative from a fatigue-life perspective, since a higher predicted da/dN gives a shorter predicted life. However, the rate comparison should be interpreted only qualitatively. The Paris parameters were not calibrated for Bold's rail steel under sequential mixed-mode loading, and the same material constants were used for both mode I and mode II contributions.

The discrepancy could also be related to the simplified interaction between the mode I and mode II parts of the cycle. Bold showed that the coplanar growth rate cannot be described as a purely independent mode II contribution. The mode I part of the cycle can influence the subsequent mode II growth by changing the residual crack opening and thereby the level of frictional resistance along the crack faces. This means that a rate law based only on simplified combinations of ΔK_I and ΔK_{II} cannot be expected to reproduce the experimental rates quantitatively.

In addition, the experiment includes crack face contact during the fully reversed mode II part of the loading. The present FE model includes normal crack face contact, but does not explicitly account for frictional resistance, oxide formation, wear debris, or crack face roughness. These mechanisms may reduce the effective mode II sliding at the crack tip and thereby lower the experimental crack growth rate compared with the numerical estimate.

The crack was also propagated freely from the initial crack. The predicted directions and resulting crack path are shown in Figure 3.32. The original VCTD formulation with $\psi = 0.01$ was excluded from the propagated path analysis because it predicted an unsatisfactory initial direction in the stationary evaluation and was not prioritized, seen in Figure 3.30b.

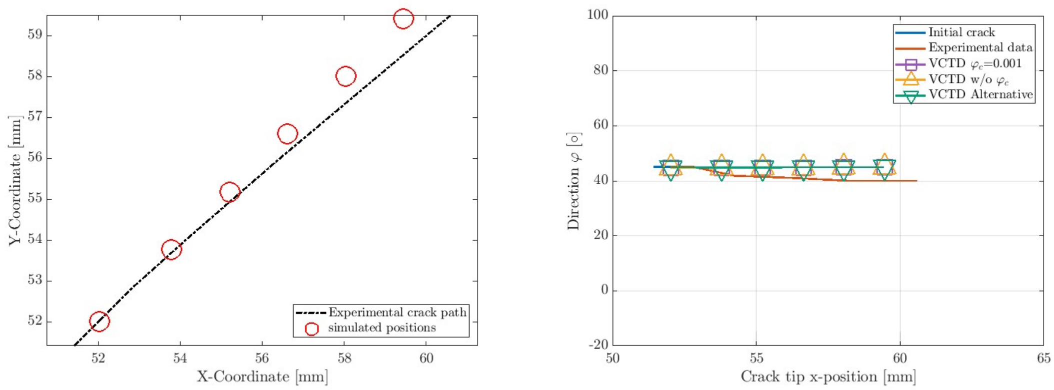

(a) **(b)**

Figure 3.32: "RSB8" predictions obtained by freely propagating the crack. (a) Crack path. (b) Crack growth direction.

The predicted crack path is almost perfectly coplanar. This should not necessarily be interpreted as an error in the predicted path. In the idealized FE model, the geometry, material response and loading are symmetric with respect to the original crack plane. A straight coplanar crack is therefore a reasonable response for a homogeneous linear elastic material subjected to this prescribed sequential loading.

The experimental crack path shows a small curvature of approximately 5°. This deviation may originate from effects not included in the present model, such as residual plastic deformation from previous cycles, crack face roughness, oxide and wear debris, local material heterogeneity, small loading asymmetries, or uncertainty in digitizing the crack path. Since the deviation is small, the freely propagated results are satisfactory.

The rates was also computed over the propagating cycles, using the same material parameters as for the instances of the experimental path. The rates were then compared with the crack growth rates reported by Bold [26], seen in Figure 3.33.

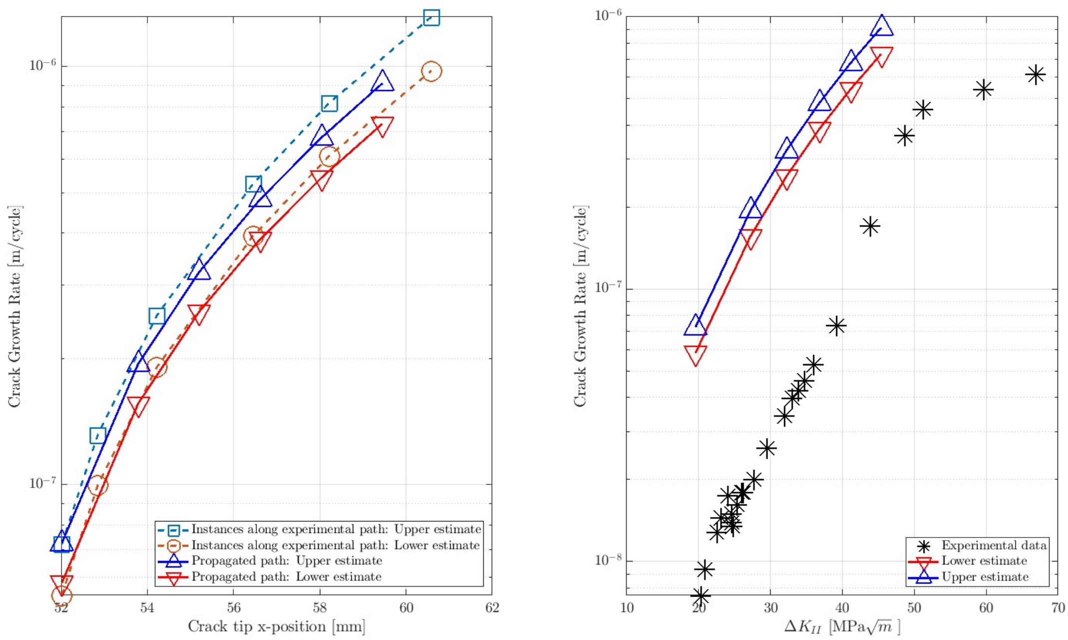

(a) **(b)**

Figure 3.33: "RSB8" crack growth rate estimates for the freely propagated path. (a) Lower and upper estimates. (b) Rate plotted against ΔK_{II}.

The growth rates obtained from the freely propagated crack are consistent with those obtained along the experimentally prescribed path. This is expected because both crack paths remain close to coplanar, giving similar crack tip loading histories. The predicted rates remain higher than the experimental values for the same reasons discussed for the stationary path evaluation, the Paris parameters are not calibrated for the present material and loading sequence, and the simplified rate formulation does not explicitly account for crack face friction, locking, oxide formation, or wear debris. The agreement between the stationary and freely propagated rates therefore supports the consistency of the numerical procedure, but it should not be interpreted as quantitative validation of the rate model.

Using the estimated crack growth rates, the fatigue life was obtained by integrating the crack growth rates (da/dN) along the propagated crack path, as described in Section 2.3. The resulting number of cycles is compared with the experimental value reported by Bold in Figure 3.34.

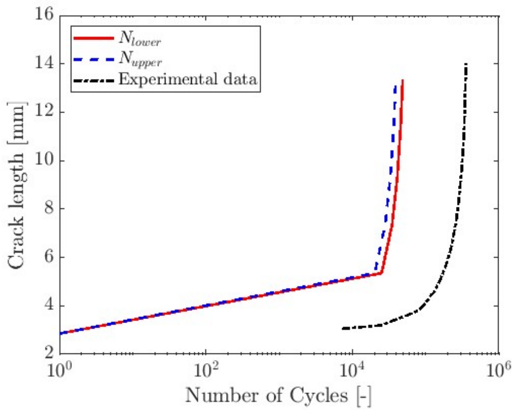

Figure 3.34: Estimated crack evaluation with cycles for the "RSB8" experiment

The predicted fatigue life is shorter than the experimental life because the crack growth rates are overestimated. The life estimate could therefore be seen as conservative. However, this conservatism should not be interpreted as a validated safety margin, since it follows mainly from limitations in the rate model and from the use of non calibrated Paris parameters. A quantitative life prediction would require a rate formulation calibrated for sequential mixed-mode loading in rail grade steel, preferably including the effect of crack face contact and frictional losses.

3.3.2.2 Sensitivity

Sensitivity studies were performed for "RSB8" using the same interpretation as for the other experiments, the aim is to verify that the predicted crack growth direction is not controlled by the chosen time step or crack tip element size. The time step sensitivity is summarized in Table 3.8.

Table 3.8: Time step sensitivity for the VCTD formulations fo the "RSB8" experiment.

Time step size [s]	VCTD $\psi = 0.01$ φ [○]	VCTD $\psi = 0.001$ φ [○]	VCTD w/o ψ φ [○]	Alt. VCTD φ [○]
$\Delta t = 0.0010$	-33.5876	0.3588	-0.2157	-0.0679
$\Delta t = 0.0025$	-33.5619	-0.1950	-0.1950	-0.0678
$\Delta t = 0.0050$, ref	-33.5300	-0.1686	-0.1686	-0.0678

Reducing the time step from the reference value produced negligible changes in the accumulated predicted angle, with deviations below 1°, for the different formulations of the VCTD criterion. The chosen time step is therefore sufficiently small for the "RSB8" load cycle evaluation.

The mesh size sensitivity is summarized in Table 3.9.

Table 3.9: Mesh size sensitivity for the VCTD formulations of the "RSB8" experiment.

Element size near crack tip [mm]	VCTD $\psi = 0.01$ φ [$\circ$]	VCTD $\psi = 0.001$ φ [$\circ$]	VCTD w/o ψ φ [$\circ$]	Alt. VCTD φ [$\circ$]
$h_c = 0.03$	-33.4816	-30.4438	-0.0148	-0.0058
$h_c = 0.05$, ref	-33.5300	-0.1686	-0.1686	-0.0678
$h_c = 0.10$	-33.1491	-0.0993	-0.0993	-0.0401

The mesh sensitivity study shows that the formulations without a reversed shear threshold are essentially mesh independent for the investigated element sizes. Both the VCTD formulation without ψ and the alternative VCTD formulation give deviations smaller than 1° relative to the reference mesh. These deviations are small compared with the experimental uncertainty and do not affect the interpretation of the results.

In contrast, the formulation with $\psi = 0.001$ shows a strong sensitivity for the finest mesh, where the predicted angle changes from approximately 0° to about $-30°$. This indicates that threshold-based reversed shear filtering can introduce a discontinuous numerical effect, where small changes in the near tip displacement field may determine whether a reversed shear increment is included or excluded from the accumulated crack-driving vector. This sensitivity is particularly important for "RSB8", since the crack is close to contact during part of the fully reversed mode II loading. The mesh study therefore supports using either the formulation without ψ or the alternative VCTD formulation for the "RSB8" propagation analysis.

The sensitivity to the evaluation distance (d_h) was also investigated, since the VCTD criterion is evaluated from relative crack face displacements at a finite distance behind the crack tip. The distance must be small enough to represent the local crack tip field.

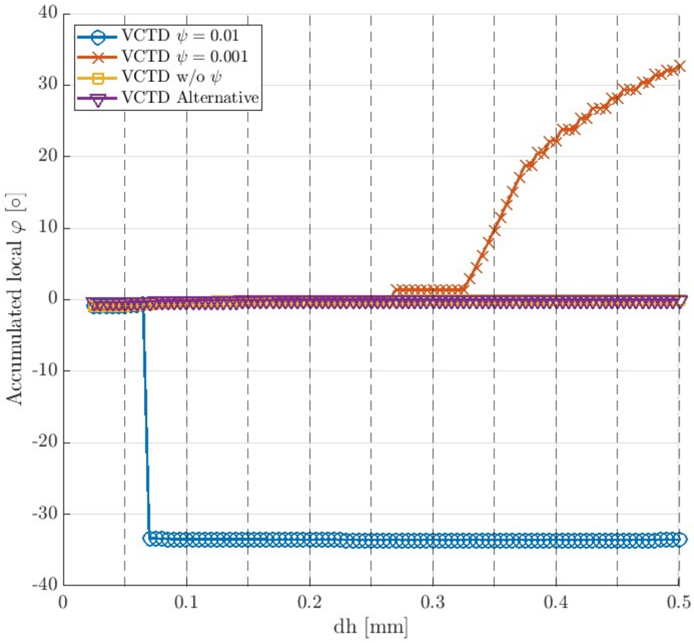

Figure 3.35: Sensitivity of evaluation point along crack faces for the "RSB8" experiment.

The predicted direction for the different formulations can be seen to be sensitive of chosen distance (d_h). The dotted lines represents the elements, where small variations of the predicted direction appears in the third to fifth element, with deviation of $< 1°$. Larger variations is shown in the first to second element and further away from the crack. This was why a measured distance of $d_h = 0.145$ mm was used.

The ABAQUS contour dependence of the SIF ranges was also investigated. The results are shown in Figure 3.36.

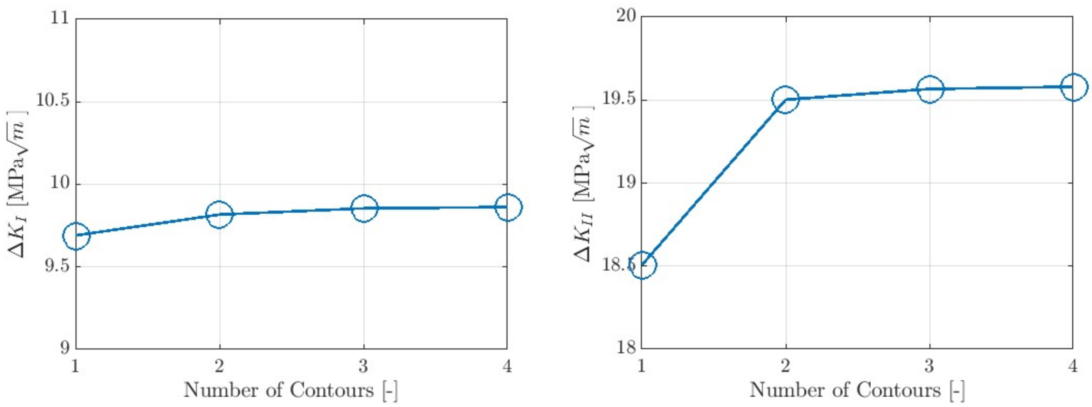

(a) **(b)**

Figure 3.36: Sensitivity of chosen contour in ABAQUS on obtained SIF ranges of the "RSB8" experiment. (a) ΔK_I (b) ΔK_{II}

The mode I range is stable from approximately the second contour, while the mode II range becomes more stable from approximately the third contour. The third contour was therefore selected for the rate estimates.

3.3.3 RSB3

In the "RSB3" experiment, the crack initially grows in shear mode and then kinks into a more mode I dominated branch. This means that the criterion must not only represent growth along an established crack plane, but also capture a transition between growth modes. In this experiment, fully reversed mode II loading is superimposed on a static mode I load with respect to the initial 45° crack, see Figure 3.25b, where the static mode I component promotes crack opening and reduces crack face contact.

3.3.3.1 Results and Discussion

As for the "RSB8", experiment was the crack face displacements (δ_I, δ_{II}) evaluated at a distance $d_h = 0.145$ mm from the crack tip.

Predictions were first obtained at six instances along the experimentally observed RSB3 crack path. The results are shown in Figure 3.37.

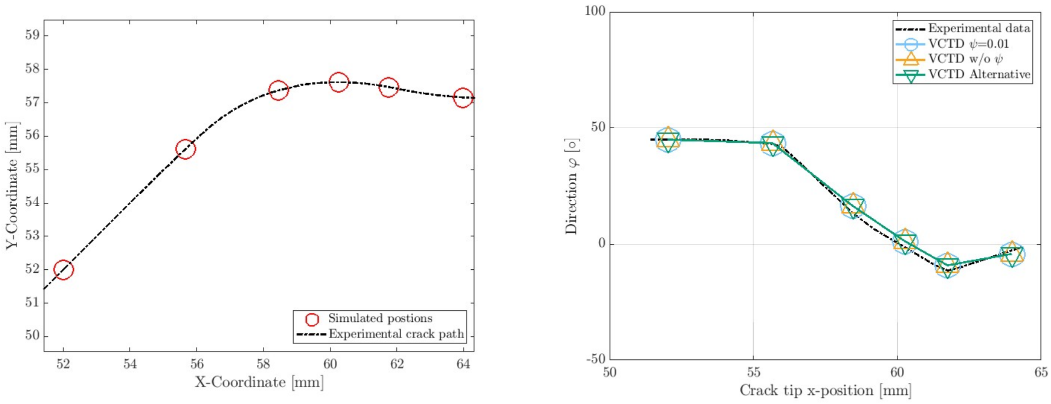

(a) **(b)**

Figure 3.37: "RSB3" predictions evaluated along the experimentally observed crack path. (a) Crack path. (b) Crack growth direction.

The different VCTD formulations give similar predictions along the experimentally prescribed path. In contrast to "RSB8", the crack tip response along the kinked "RSB3" path is more strongly influenced by opening, and the reversed shear contribution is therefore less important. The predicted directions correlate well with the experimental path, although somewhat larger deviations occur around the part of the path where the crack direction changes most rapidly.

The crack growth rate estimates along the experimentally prescribed path are shown in Figure 3.38. The same material parameters as for "RSB8" were used, since there were no reported parameters in the experiment.

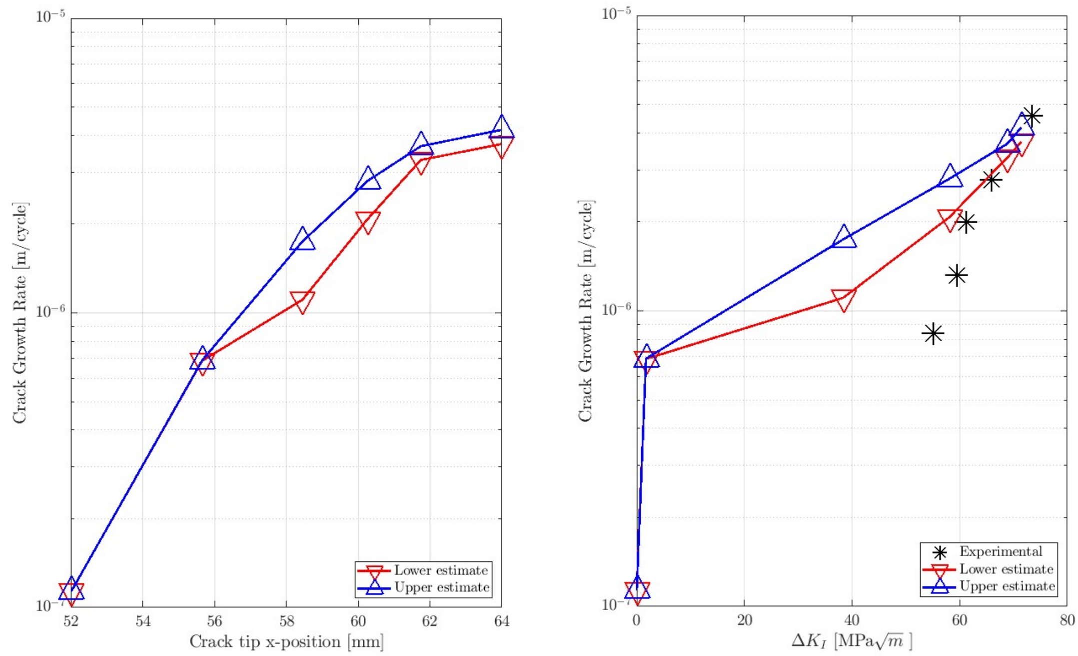

(a) **(b)**

Figure 3.38: "RSB3" crack growth rate estimates along the experimentally prescribed path. (a) Lower and upper estimates. (b) Rate plotted against ΔK_I.

For the initial straight part of the crack, the lower and upper rate estimates coincide. At this stage, the crack remains close to the original 45° orientation and the mode I component is mainly static, so the cyclic mode I range is small or close to zero. The crack growth rate is therefore governed primarily by the mode II range. As the crack starts to kink, the local crack orientation changes and the originally static opening load begins to contribute more strongly to the cyclic crack tip loading of the branch. The mode I range therefore increases, and the lower and upper estimates begin to separate.

The experimentally reported rate data were limited, but the behavior could be seen as consistent with the experimental interpretation of "RSB3". Bold observed that the crack initially grew in mode II, but that mode I branch growth eventually dominated [26]. The rate estimates along the prescribed path therefore reflect the change in local crack tip loading caused by the experimentally imposed kink. However, uncertainty remains because the experimental path is digitized from an image, and small errors in local crack angle can produce significant changes in the extracted SIF ranges. As mentioned for "RSB8" experiment, the material parameters and simplified rate models are sources of discrepancy

The crack was then propagated freely from the initial crack using the VCTD formulations. The resulting predictions are shown in Figure 3.39.

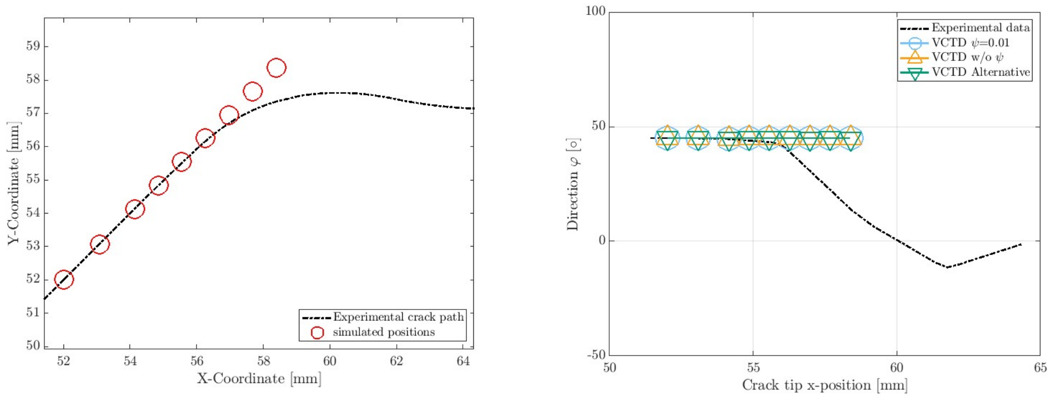

(a) **(b)**

Figure 3.39: "RSB3" predictions obtained by freely propagating the crack. (a) Crack path (b) Crack growth direction.

In contrast to the evaluation of the path following the experiment, the freely propagated simulation does not reproduce the experimentally observed kink. Instead, the predicted crack continues approximately along the original 45° direction. This is an important result, the present VCTD implementation can follow the kinked experimental geometry when that geometry is prescribed, but it does not independently trigger the transition from shear mode to tensile mode growth.

One possible explanation is that, in the idealized two-dimensional model, the geometry, material and loading are nearly symmetric. Under such conditions, upward and downward deviations from the original crack plane may be mechanically similar, and the numerical model contains no physical imperfection that forces the crack into the experimentally observed downward branch. In the real specimen, small imperfections such as microstructural inhomogeneity, crack front curvature, local roughness, residual plasticity or slight loading misalignment may break this symmetry and initiate branching.

Pascoe and Smith performed a similar experiment on HY100 steel using cruciform specimens subjected to cyclic shear loading with an equibiaxial mean stress [27]. In contrast to Bold's rail-steel experiments, they reported continuous mode II growth. This suggests that the transition from shear-mode growth to mode I branching in "RSB3" is not controlled by the loading condition alone, but also by the material response.

Bold [26] argued that the discrepancy between the HY100 results and the rail-steel results was presumably related to differences in the fatigue behavior of the materials. This interpretation is also consistent with observations from torsional fatigue tests, where different alloys have been shown to favor different crack growth modes under similar loading conditions. In this context, the tendency of the "RSB3" crack to kink into a tensile-mode branch may be influenced by the chemical composition and microstructure of the rail steel, as well as by its cyclic plasticity, crack face roughness, and residual stresses. These effects are not represented in the present homogeneous linear elastic model. The freely propagated simulation may therefore continue along the shear-mode direction even though the physical experiment develops a competing tensile-mode branch.

The crack growth rate estimates for propagated crack are shown in Figure 3.40.

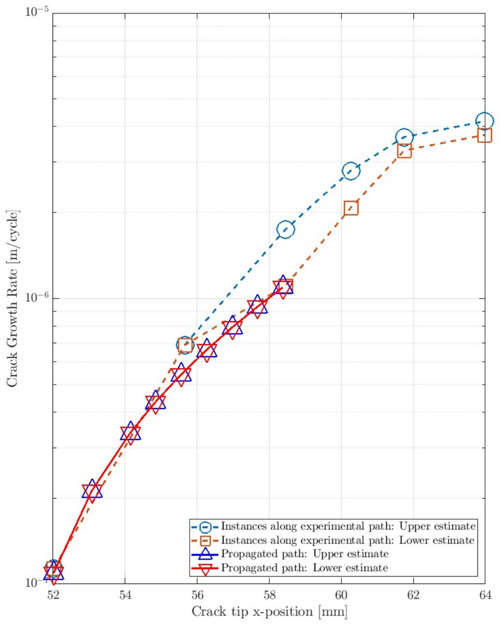

(a)

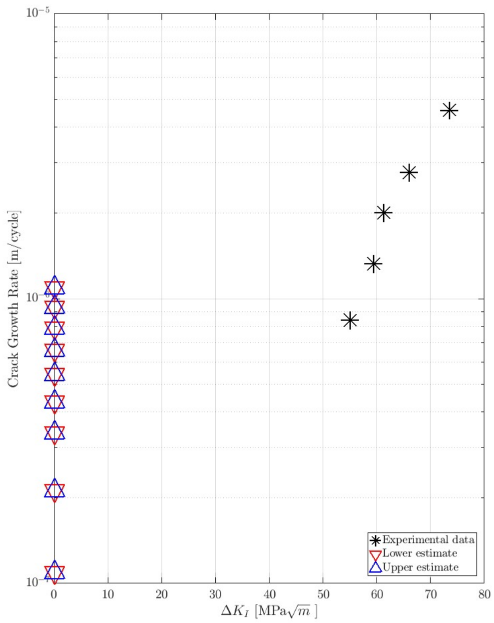

(b)

Figure 3.40: "RSB3" crack growth rate estimates for the freely propagated path. (a) Lower and upper estimates. (b) Rate plotted against ΔK_I.

The crack growth rate comparison for "RSB3" must be interpreted in relation to the predicted crack path. Along the experimentally prescribed path, the crack kinks into a direction where the mode I contribution becomes more important. Along the freely propagated numerical path, however, the crack remains close to the original 45° direction, where the loading remains predominantly shear dominated. The two analyses therefore do not correspond to the same crack tip loading history.

This explains why the propagated path rate may appear inconsistent when plotted against the experimentally reported ΔK_I values. The experimental crack has already entered a more ΔK_I dominated branch, whereas the numerically propagated crack remains in a configuration where ΔK_I is small or nearly constant and the shear contribution remains dominant. The discrepancy in the rate plot is therefore partly a consequence of the path discrepancy.

For this reason, the "RSB3" rate prediction was not further used for fatigue life estimation. The results instead show that prediction of direction and rate prediction are strongly coupled, a deviation in path usually results in a higher deviation in SIF history, which in turn leads to an incorrect rate comparison due to power relation in Paris law.

The most likely explanation is that the present model treats the crack as a single continuously propagating path, whereas the experiment may involve competition between coplanar shear mode growth and a separate tensile mode branch. Additional effects such as residual plasticity, crack face roughness, local microstructural heterogeneity and small experimental asymmetries may also contribute. Capturing the "RSB3" transition would therefore likely require either an explicit branching criterion or a propagation algorithm that evaluates multiple candidate crack extensions.

3.3.3.2 Sensitivity

The sensitivity study for RSB3 is particularly important because it helps determine whether the missing experimental kink is caused by insufficient numerical resolution or by modeling assumptions. If the predicted initial direction were strongly dependent on time step, mesh size or evaluation distance, the absence of kinking could be a numerical artifact. If the prediction is insensitive to these parameters, the discrepancy is more likely related to the physical assumptions of the model or to the crack growth criterion itself.

Table 3.10: Time step sensitivity for the VCTD formulations for the "RSB3" experiment.

Time step size [s]	VCTD $\psi = 0.01$ φ [$\circ$]	VCTD w/o ψ φ [$\circ$]	Alt. VCTD φ [$\circ$]
$\Delta t = 0.0010$	3.2137e-06	3.2137e-06	1.2611e-05
$\Delta t = 0.0025$	-4.0118e-06	-4.0118e-06	1.2611e-05
$\Delta t = 0.0050$, ref	-7.2320e-07	-7.2320e-07	6.5248e-06

The time step sensitivity is negligible. All three formulations predict an initial direction close to zero relative to the original crack plane for the investigated time steps.

The mesh size sensitivity is summarized in Table 3.11.

Table 3.11: Mesh size sensitivity for the VCTD formulations for the "RSB3" experiment.

Element size near crack tip [mm]	VCTD $\psi = 0.01$ φ [○]	VCTD w/o ψ φ [○]	Alt. VCTD φ [○]
$h_c = 0.03$	2.8757e-06	2.8757e-06	-1.0323e-06
$h_c = 0.05$, ref	-7.2320e-07	-7.2320e-07	6.5248e-06
$h_c = 0.10$	4.8957e-06	4.8957e-06	-1.5273e-05

The mesh sensitivity study also shows negligible variation in the predicted initial direction. Refining the crack tip element size from $h_c = 0.10$ mm to $h_c = 0.03$ mm does not influence the results. This supports the conclusion that the missing kink is not primarily a mesh resolution problem.

The influence of the evaluation distance (d_h) is shown in Figure 3.41.

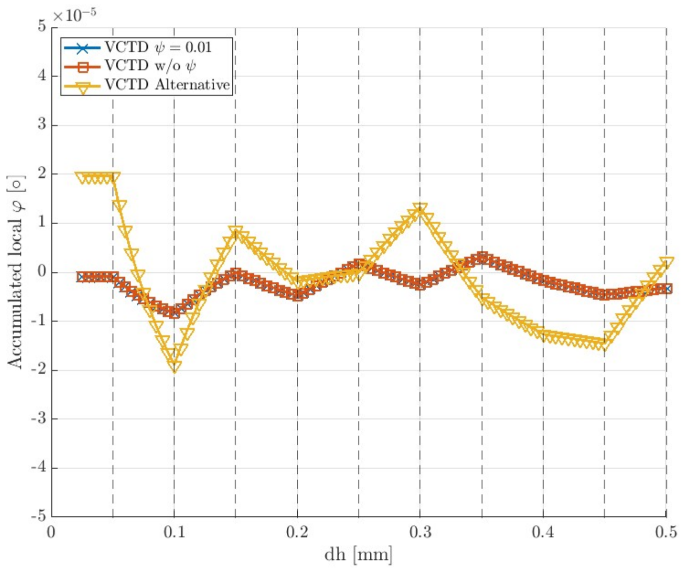

Figure 3.41: Sensitivity of evaluation point along crack faces for the "RSB3" experiment

The first evaluation points closest to the crack tip show some local variation, while the prediction stabilizes further away from the tip. The overall deviation remains negligible and does not affect the results. The evaluation point should nevertheless not be placed too far from the crack tip, since the displacement field may then be influenced by higher order terms and the global specimen response rather than by the local crack tip field [17]. Therefore, the crack face displacements were evaluated at $d_h = 0.145$ mm.

The ABAQUS contour dependence of the SIF ranges is shown in Figure 3.42.

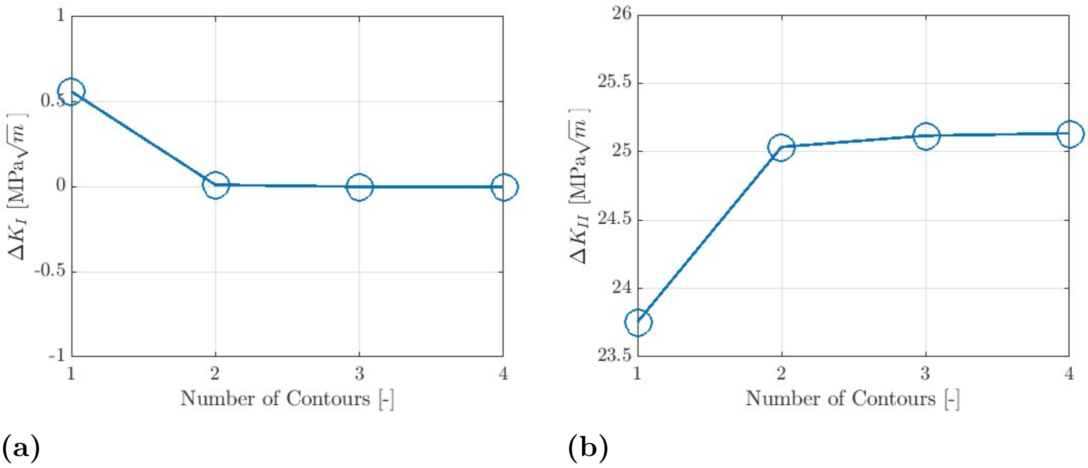

Figure 3.42: Sensitivity of chosen contour in ABAQUS on obtained SIF ranges of the "RSB3" experiment. (a) ΔK_I (b) ΔK_{II}

The SIF ranges are stable after approximately the second contour for ΔK_I and the third contour for ΔK_{II}, extracting the ranges from the third contour therefore seemed satisfactory.

This indicates that the extracted rate quantities are not dominated by the selection of contours. More importantly, the combined sensitivity studies show that the missing kink in the freely propagated "RSB3" simulation is not caused by time step size, mesh size ot evaluation distance. The discrepancy is therefore more likely related to the modeling assumptions, especially the use of a homogeneous linear elastic material model and a single path crack propagation framework.

3.4 Twin-disc

To predict the direction of crack growth in rolling contact fatigue cracks in wheels and rails, an analysis on twin-discs was carried out. The current study is compared to the results of the twin-disc fatigue crack growth experimented originally carried out by Fletcher et al, labeled as "GO" in the experiments [28], where the experiment is illustrated in Figure 3.43.

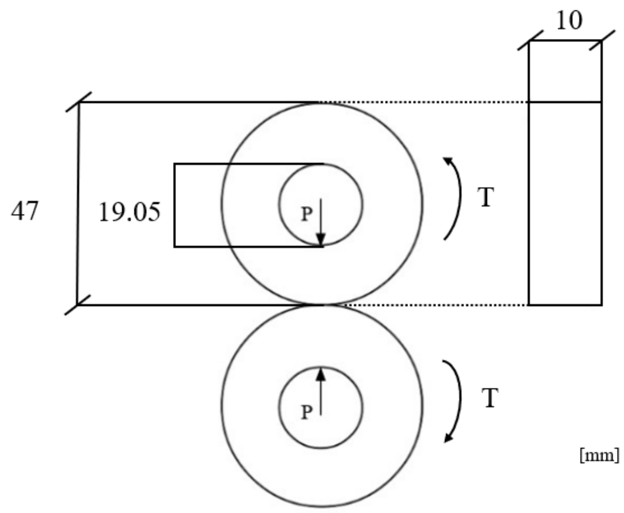

Figure 3.43: Twin-disc experimental setup explained in [28].

During the experiments, 500 unlubricated cycles were applied to induce damage to the specimen, followed by 30 554 cycles using the lubricant "graphite in mineral oil" between the rail and wheel discs. The tests were conducted on a Twin-disc rolling-sliding contact simulation machine, employing a maximum Hertzian contact pressure of 1500 MPa, and the traction coefficient during the lubricated phase between the wheels and rails was measured as $\mu_{wr} = 0.04$. Once the experiment was complete, a crack with the length of 900 μm and depth of 280 μm was found. The wheel and the rail were treated be made by rail steel UIC grade 900A steel and have the Young's modulus and Poisson ratio of E = 210GPa and $\nu = 0.3$, respectively.

3.4.1 FE-setup

In order to represent the rail, a rectangle with the width of 20 mm and height of 10 mm was created. A frictionless crack of the length $a_0 = 450\mu m$ at an incline of $\varphi_0 \approx -18°$ was first embedded in the upper middle part of the surface as an initial crack, then the crack extended to $a_{tot} = 900\mu m$ for the same incline. The specimen was simulated under plain stress conditions. Regarding boundary conditions, all nodes on the vertical sides were constrained on the x-direction and all bottom loads where constrained in the y-direction. The wheel load is applied to the top surface of the rail part sequentially and is transmitted through a contact patch (b). The boundary conditions and loads are illustrated in Figure 3.44.

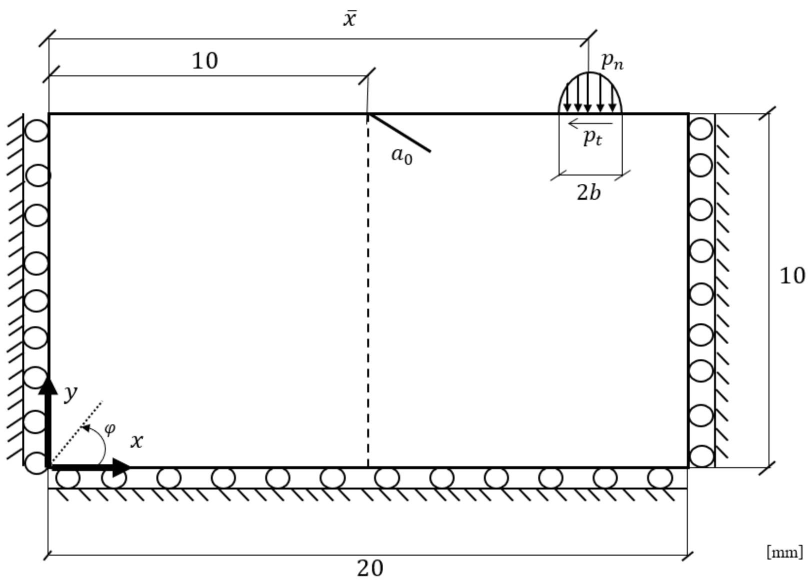

Figure 3.44: FE-setup of the Twin-disc.

The contact pressure created by a passing wheel on the rail can be approximated using Hertzian contact theory [29], where the pressure distribution is assumed to have an elliptical distribution [30]. The contact pressure distribution in the contact patch is thus defined for a given contact load position ($\bar{x}$) as

$$p_n(\bar{x}; x) = \begin{cases} \frac{2P}{\pi b^2}\sqrt{b^2 - |x - \bar{x}|} & |x - \bar{x}| < b, \\ 0 & [x - \bar{x}] \geq b, \end{cases} \tag{3.4}$$

where the maximum contact pressure is given as 1500 MPa, and P is the contact load per unit thickness and $|\cdot|$ is the absolute value [30]. Relating the contact load (P) to the contact patch (b) corresponds to

$$b = \sqrt{\frac{4PR}{\pi E^*}}. \tag{3.5}$$

The radius (R) is given by the following expression

$$\frac{1}{R} = \frac{1}{R_{wheel}} + \frac{1}{R_{rail}}, \tag{3.6}$$

where the wheel and rail radius is assumed to be the same, as in $R_{wheel} = R_{wheel} = 0.0235$ m, and E^* is the effective modulus determined as

$$\frac{1}{E^*} = \frac{1 - \nu_{wheel}^2}{E_{wheel}} + \frac{1 - \nu_{rail}^2}{R_{rail}}. \tag{3.7}$$

Using the presented contact formulae resulted in the contact magnitude $P \approx 0.72 MN/m$ and contact patch $b \approx 0.3 mm$.

Furthermore, a full-slip condition is assumed for wheel–rail traction stresses. These tangential traction stresses can therefore be given by

$$p_t(\bar{x}; x) = -\mu_{\mathrm{wr}}\, p_n(\bar{x}; x), \tag{3.8}$$

A wheel passage is simulated by moving the contact load along the top surface of the rail, where compressive stresses arise due to the wheel–rail contact. However, the crack face contact constraints need to be employed. Here, penalty formulations are applied in the FE model as described in section 2.4.

The employed FE-mesh for this experiment consists of four-node quadrilateral elements with a size of 11μm near the crack tip, as seen by Figure 3.45.

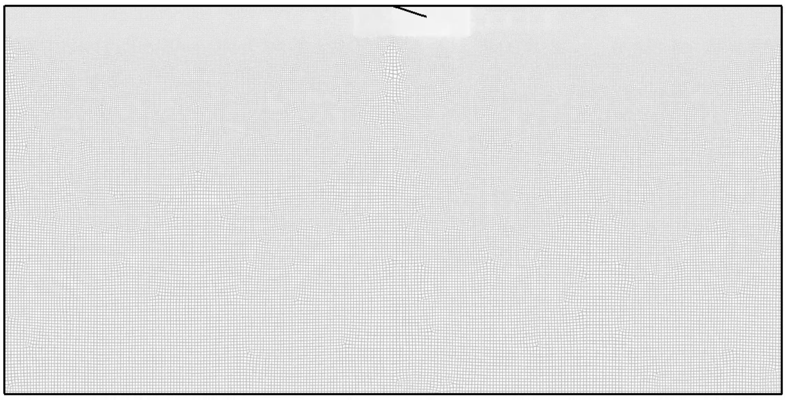

(a)

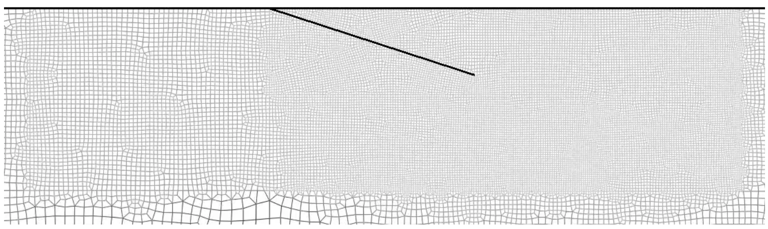

(b)

Figure 3.45: FE mesh used in simulation of Twin-disc experiment. (a) Mesh of full model. (b) Mesh zoomed in at the crack tip area.

3.4.2 Result and Discussion

The second half of the full experimental crack path is simulated, where 5 stationary positions at 0%, 25%, 50%, 75%, and 100% of the crack length was analyzed. The crack growth direction was evaluated with a distance $d_h = 52\mu$m from the crack tip. Numerical predictions at five instances along the experimentally observed crack path was compared to the simulated resulted, the points of evaluation are illustrated by Figure 3.46a, and predicted crack growth direction is shown by Figure 3.46b.

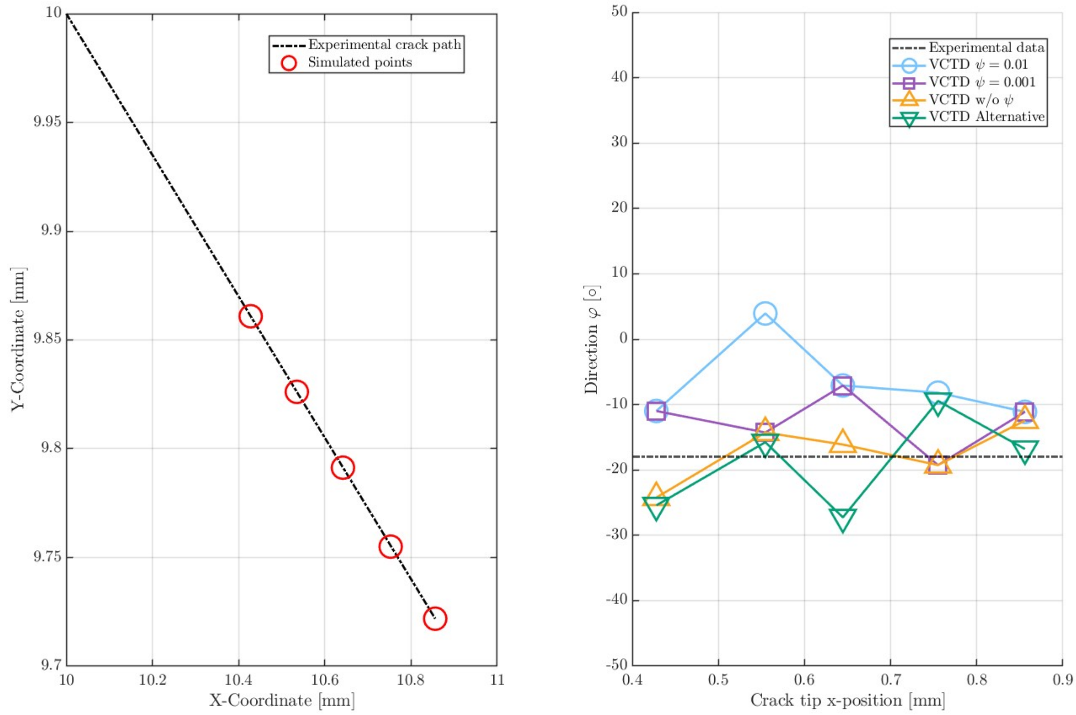

(a) **(b)**

Figure 3.46: Stationary points along the crack path for the Twin-disc experiment. (a) Stationary points along the experimental path. (b) The resulting predicted crack growth direction.

Figure 3.46 shows that the different VCTD formulations predict noticeably different crack growth directions for the Twin-disc rolling contact fatigue experiment. None of the formulations consistently reproduces the experimentally observed crack path, although the formulations with little (i.e., ψ=0.001) to no reverse shear generally remain closer to the experimental direction compared to the VCTD formulation with $\psi = 0.01$. In particular, the VCTD formulation with $\psi = 0.01$ predicts a temporary positive, i.e., kinking upwards, crack growth angle near the beginning of the simulated crack, indicating a substantially different sensitivity to local shear-driven displacement contributions. This behavior can be related to the reverse shear condition in Equation (2.9), where a larger ψ requires a higher ratio of $\delta_I/|\delta_{II}|$ for reverse shear to be activated. As a result, fewer reverse shear events contribute to the accumulated damage, which reduces the influence of shear fluctuations on crack growth. In contrast, smaller values of ψ allow more frequent activation of reverse shear [31]. Additionally, the choice of d_h influences the evaluated displacement field and may contribute to the observed variation in predicted crack growth direction. A dedicated sensitivity study of this parameter is recommended for future work. However, the VCTD criterion without ψ and the alternative formulation yield closely matching predictions, supporting the observation that excluding reverse shear contributions leads to a consistent crack growth response. The discrepancy between the formulations is likely associated with the strongly mixed-mode loading conditions present in rolling contact fatigue, where crack face interaction and shear-driven propagation become more significant. This suggests that crack growth predictions are highly sensitive to the treatment of reverse shear instances under mixed-mode loading conditions. Additionally, the predictions are also influenced by numerical aspects of the FE model, including contact enforcement, and the extraction of crack tip displacement components under highly compressive mixed-mode loading.

In order to compare the number of cycles to failure found by Fletcher et al. [28], the predicted crack growth rates were integrated between multiple crack path positions. The crack growth rates were estimated using the Paris law constants C = $2.47\times10^{-9}\ \frac{mm/cycle}{MPa\sqrt{m}}$ and m = 3.33 for rail steel UIC grade 900A[32], yields the results in Figure 3.47.

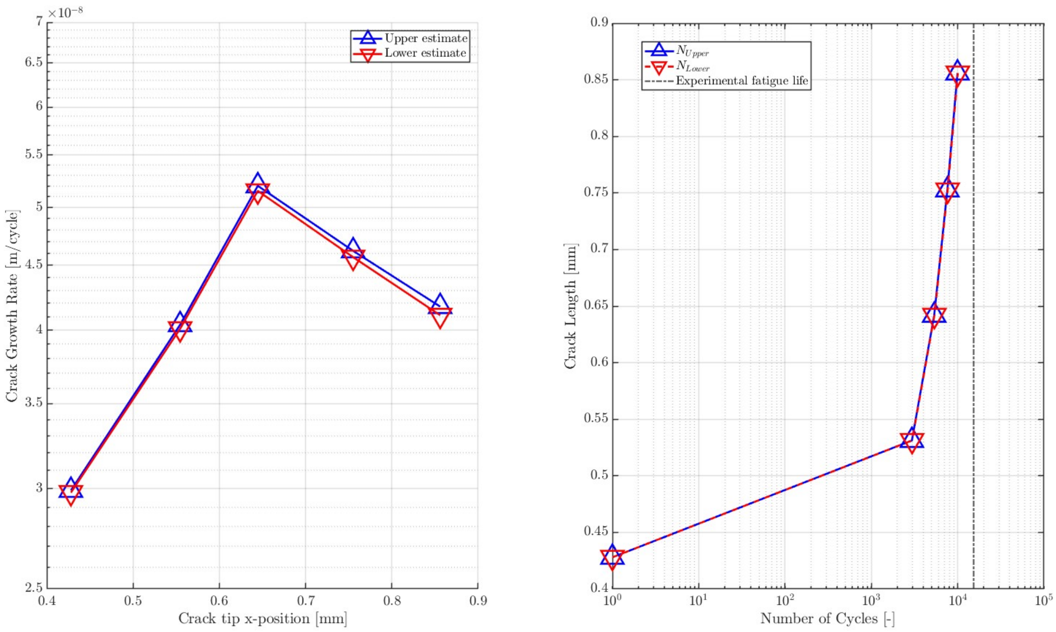

(a) **(b)**

Figure 3.47: Fatigue life for the Twin-disc experiment. (a) Crack growth rate. (b) Estimated number of cycles until failure.

The crack growth rate estimates are presented in Figure 3.47a, showing crack initially exhibit a higher growth rate, before decreasing at larger crack lengths. This trend can be attributed to the stress field location as a result of the loading on top of the surface of the rail. Short cracks are embedded within regions of higher stress concentration, as the positions lay closer to the applied load, resulting in a higher crack growth rate. As the crack length increases, the crack tip experiences progressively lower stresses due to stress field being further away from the loading region. It should also be noted that there is a visible difference between the upper and lower estimated bounds for the crack growth rate, this is due to the fact that there is mixed mode loading conditions present in the experiment. The predicted number of cycles show a shorter fatigue life compared to that reported by Fletcher et al. [28], as seen in Figure 3.47b. The experimental values correspond to half of the reported number of cycles, as only the second half of crack growth is simulated in the present study. One possible explanation for this discrepancy is that the crack growth rate increases with crack length, consistent with the nonlinear nature of fatigue crack propagation and Paris' law [1], [6]. As a result, most of the fatigue life is consumed at shorter crack lengths rather than scaling linearly with crack extension. Additional differences may arise from the exclusion of the early crack growth stage and from modelling assumptions in the numerical formulation. The influence on the Paris Law constants (C and m) may also contribute to the discrepancy in fatigue life predictions. These material constants are determined experimentally and are known to vary depending on the material condition, heat treatment, manufacturing process, and testing environment. Since the exact material state of the steel used in the experiments may not be fully reproduced in the numerical model, deviations in crack growth behavior are expected [1].

Next is the predicted crack growth direction given by the propagating points where the crack growth length was $l = 0.15$mm. The predicted directions and their resulting crack path are shown in Figure 3.48. The original VCTD formulation with $\psi = 0.01$ was excluded from the propagated-path analysis due to the fact that it predicted an unrealistic positive kinking in the stationary evaluation. Figure 3.48a shows the protected crack growth direction and Figure 3.48b shows the resulting positions given by the different VCTD formulations.

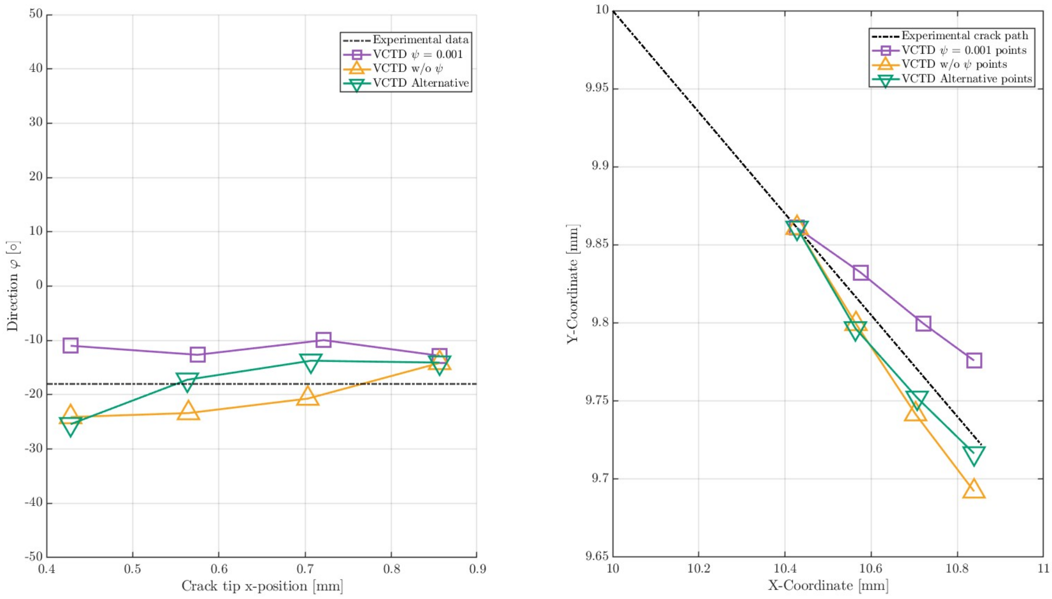

(a) **(b)**

Figure 3.48: Propagating points for the Twin-disc experiment. (a) Points propagated for the different VCTD criterion. (b) Resulting predictive crack growth directions.

As illustrated in Figure 3.48, the predicted crack growth directions differ depending on the VCTD criterion. It is evident that the formulations with little (i.e., ψ=0.001) or no reverse shear generally predict crack propagation paths that remain closer to the experimentally observed trajectory. Once again, the VCTD criterion without ψ and the alternative formulation yield closely matching predictions, indicating a consistent crack growth response when reverse shear effects are excluded. Where the alternative formulation has the best match.

Overall, the differences between criteria are less pronounced for the propagation paths compared to the stationary point evaluation, where all formulations remain in closer agreement with the experimental crack trajectory. This suggests that the propagation-based evaluation exhibits a reduced sensitivity to local variations in the crack tip state, as the crack growth direction is evaluated over successive increments rather than at isolated stationary configurations.

The number of cycles to failure found by Fletcher et al. [28] is compared again for contour 3, however, the experimental data is now compared with the propagating points given as a result of the different VCTD criterion, as illustrated in Figure 3.49.

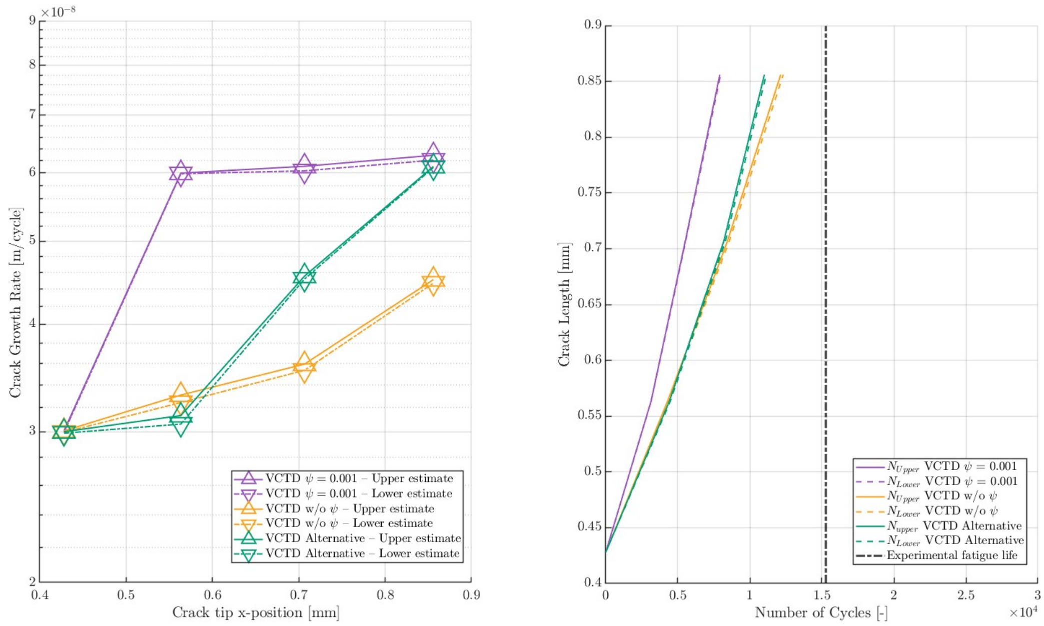

(a) **(b)**

Figure 3.49: Fatigue life estimation for predictive points given by VCTD $\psi = 0.001$, VCTD without ψ, and the alternative VCTD formulation for the Twin-disc experiment. (a) Crack growth rate. (b) Predicted number of cycles.

Figure 3.49a shows how the VCTD formulations estimate the different crack growth rates as a result of the propagation provided by the predicted crack growth direction. During the early stages of propagation, the formulation without ψ and the alternative VCTD formulation predict growth rates of the same magnitude. However, as the crack advances, the estimates begin to diverge, with the formulation incorporating $\psi = 0.001$ predicting notably higher growth rates. A consistent difference between the upper and lower bound estimates is also observed across all formulations, reflecting the influence of mixed-mode loading conditions on the predicted crack growth direction. Compared to the stationary crack growth estimates, which exhibit an initial rise followed by a decline in crack growth rate with increasing crack tip position, the propagating crack formulations predict a more sustained increase across the crack. This difference can be attributed to the evolving crack geometry in the propagating case, which continuously updates the crack configuration and thus the estimated growth rates, whereas the stationary crack follows a fixed path. The associated fatigue life is presented in Figure 3.49b, where the fatigue life prediction is similar during the early stages of propagation. However, as the crack propagates, the predictions begin to deviate. The formulation with $\psi = 0.001$ predicts a steeper increase in crack growth rate, indicating a shorter fatigue life, whereas the formulation without ψ produces lower growth rates over most of the crack path, which then estimates a longer fatigue life. The alternative VCTD approach initially follows the lower-growth trend but exhibits a sharper increase at larger crack lengths, also leading to reduced fatigue life. It should, however, be mentioned that neither of the predicted fatigue life are close to the experimental estimate. This may be attributed to the increase in crack growth rate with crack length, consistent with the nonlinear nature of fatigue crack propagation [1], and the Paris Law constants. As shown in Figure 3.48, even slight changes in the estimated crack growth direction significantly influence the total crack trajectory and, consequently, the number of cycles to failure. This highlights that an accurate estimation of the crack growth direction is essential for reliable fatigue life predictions.

3.4.3 Sensitivity

Once again, a sensitivity study was preformed in order to evaluate the robustness of the experiment.

The contour sensitivity study was is represented in the Figure 3.50, where the contours and resulting accuracy for the ranges of the SIFs obtained from ABAQUS are shown.

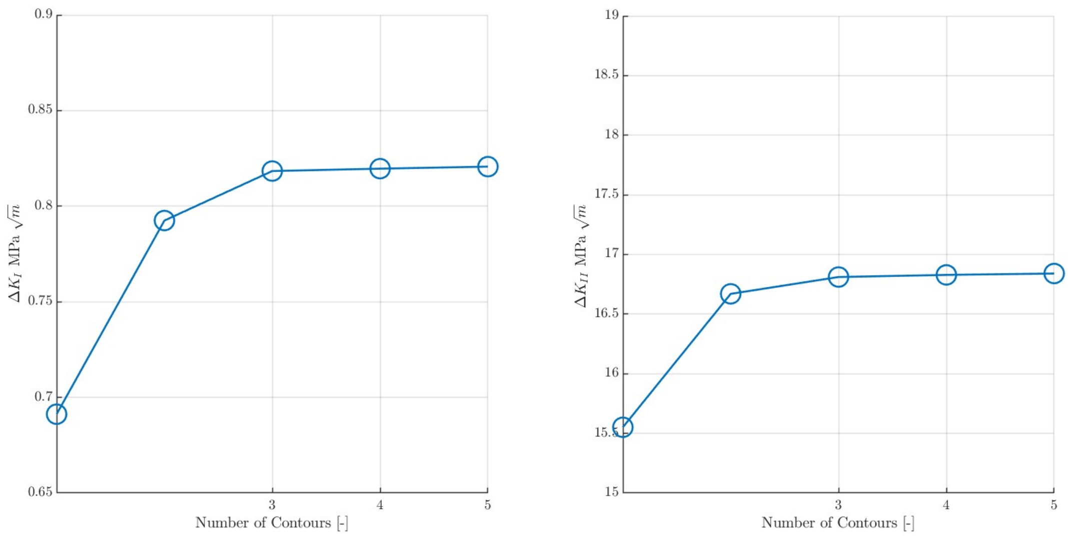

(a) **(b)**

Figure 3.50: Sensitivity of chosen contour in ABAQUS on obtained SIF ranges of the Twin-disc experiment. (a) ΔK_I (b) ΔK_{II}

From figure 3.50, it is evident that the results show an increasing trend with the number of contours, however the variations between the contours have a small difference, and the solution can therefore be considered sufficiently converged already at 3 contours.

A mesh sensitivity study was conducted, in which different mesh sizes in the vicinity of the crack tip was investigated, this was done for the initial crack, the resulting accumulated crack growth direction for different mesh size is presented in the Table 3.12.

Table 3.12: Mesh size sensitivity for the VCTD formulations.

Element size near crack tip [μm]	VCTD $\psi = 0.01$ φ [$\circ$]	VCTD $\psi = 0.001$ φ [$\circ$]	VCTD w/o ψ φ [$\circ$]	Alt. VCTD φ [$\circ$]
$h_c = 5$	6.9881383	6.9881383	-5.25583145	-6.2677198
$h_c = 11$	7.01605097	7.01605097	-6.22934355	-7.42289624
$h_c = 17$	8.45949728	8.45949728	-6.09857870	-7.29380524

As shown in Table 3.12, the accumulated crack growth direction exhibits only minor variations with mesh refinement for most criteria, where the largest deviation reported was below 2°. It should be noted that the mesh sensitivities for VCTD with $\psi = 0.01$ and $\psi = 0.001$ are identical. One possible reason is that the influence of ψ is mainly confined to the initial stage of crack propagation near the initial crack tip, after which the crack growth direction becomes governed predominantly by the global stress field, leading to nearly identical crack paths across different mesh densities. Based on the mesh sensitivity study, a mesh size of h_c= 11μm was selected for subsequent analyses, as it provides solution stability.

4

Conclusion and Future Work

This chapter presents the main conclusions of the thesis and outlines key findings from the evaluation of the different VCTD formulations. In addition, it discusses limitations of the current framework and provides recommendation for future work.

4.1 Conclusions

The objective of this thesis was to evaluate the predictive capability of different formulations of the Vector Crack Tip Displacement (VCTD) criterion, which is used for mixed-mode fatigue crack growth direction. Crack growth evaluations are complemented with crack growth rate and the resulting number of cycles to failure where applicable. Finite element models were developed for experimentally validated cases from the literature, including both stationary crack configurations and freely propagated cracks. The considered experiments covered mode I dominated mixed-mode loading, stable shear mode growth, shear-mode growth followed by kinking, and rolling contact fatigue conditions.

Overall, the results show that the VCTD framework is capable of predicting crack growth direction when the crack path evolves smoothly and when the dominant crack tip displacement mechanism is represented in the model. This was observed for the Four Point Bending (FPB), Compact Tension Shear (CTS), RSB8 and Twin-Disc experiments, where the predicted directions generally followed the experimentally observed trends.

For mode I dominated cases, the different VCTD formulations gave nearly identical predictions. This is expected because the crack opening displacement (δ_I) dominates over the sliding displacement (δ_{II}), making the treatment of reversed shear less influential. In these cases, the alternative VCTD formulation did not lead to a significantly different prediction, since the crack growth direction was mainly governed by opening.

A different behavior was observed for shear dominated loading. The "RSB8" experiment demonstrated that the accumulated VCTD approach can capture stable mode II dominated crack growth under non-proportional sequential loading. The formulations without restrictive reversed shear filtering predicted an almost coplanar crack path, both when evaluated along the experimentally prescribed crack path and when the crack was propagated freely. However, the results also showed that the treatment of reversed shear is important. The formulation using the reversed shear threshold $\psi = 0.01$ was less reliable for "RSB8", and the sensitivity study indicated that threshold-based filtering may introduce numerical sensitivity when the crack is nearly closed.

The "RSB3" experiment highlighted an important limitation of the present propagation framework. When the experimentally observed kinked path was prescribed in the finite element model, the VCTD formulations were able to follow the local crack growth direction reasonably well. However, when the crack was propagated freely, the model did not reproduce the experimentally observed transition from mode II growth to a mode I dominated branch. Instead, the crack continued along the original shear mode direction. It was also argued that this change in direction may not be due to the loading configuration, but instead is a reflection of microstructural behavior. This distinction shows that it may not be only the formulation of VCTD criterion, and instead could be due to material effects being neglected in the current FE model. The "RSB3" results therefore suggest that abrupt branching or kinking may require additional modeling beyond the current simplified FE model.

The Twin-Disc analysis showed that the VCTD framework has potential for rolling contact fatigue applications. The predicted crack growth directions showed overall agreement with the experimentally observed trajectory, especially when reverse shear filtering was not too restrictive. This suggests that crack tip displacements contain useful directional information even under rolling-sliding contact conditions. However, the rolling contact experiment also indicated the sensitivity to the both opening and sliding components. This is particularly important for rail and wheel applications, where crack face contact, and non-proportional loading strongly influence the local displacement field. Despite this, the criteria were capable of reproducing the overall experimentally observed crack paths.

For the FPB case, the predicted crack growth rate and fatigue life were in close agreement with the experimental data, indicating that the rate model can be effective under relatively mode I dominated conditions. For the CTS and "RSB8" cases, the crack growth rates were generally overpredicted, leading to conservative fatigue life estimates. These discrepancies are most likely related to the simplified Paris-type rate formulation, the use of non-calibrated material parameters, and the neglect of effects such as crack face friction, roughness, wear debris and residual plasticity.

For "RSB3", the freely propagated crack path did not reproduce the experimentally observed kink, and the corresponding rate and life predictions were therefore not considered quantitatively reliable. This confirms that crack growth direction and crack growth rate are strongly coupled: if the predicted crack path is incorrect, the extracted stress intensity factor history and resulting crack growth rate will also be affected.

In summary, the VCTD formulations evaluated in this thesis are promising for predicting mixed-mode fatigue crack growth direction, especially for smooth crack path evolution and stable shear mode growth. The main limitation is not the local displacement-based direction measure itself, but rather the frameworks current ability to predict the crack path when the physical experiment involves abrupt kinking, branching, material-dependent crack growth behavior or competing crack paths. Quantitative fatigue life prediction also requires further development, particularly through improved crack growth rate models and material-specific calibration.

4.2 Future Work

The results of this thesis suggest several directions for future work. First, the crack growth rate predictions should be improved by calibrating the Paris Law parameters for the specific materials and loading conditions considered. In the present work, general material parameters were used when experiment-specific constants were not available. This allowed qualitative comparison between the different simulations, but introduced uncertainty in the predicted crack growth rates and fatigue lives. Future work should therefore include experimentally calibrated rate parameters for both mode I and mode II dominated crack growth in the relevant materials.

Second, the mixed-mode crack growth rate formulation should be further investigated. The lower and upper estimates used in this thesis provide useful bounds, but they do not fully capture the interaction between opening and sliding contributions during non-proportional loading. This is particularly important for the "RSB8", "RSB3" and Twin-disc experiments, where the mode I and mode II parts of the loading cycle influence each other through crack opening, sliding and possible crack face contact. A more advanced rate formulation could improve the quantitative prediction of fatigue life.

Third, future work should further investigate the formulation of the VCTD criterion and its ability to capture abrupt changes in crack growth direction. In the present work, neither the CTS, FPB nor the "RSB3" simulations were able to reproduce the experimentally observed kinking during free propagation. Instead, the predicted cracks tended to continue along the existing crack path. This suggests that the current formulations may be limited when the physical crack growth process involves a sudden transition between growth modes, rather than a smooth rotation of the crack path. Although the origin of this limitation cannot be determined from the present results alone, the inability to capture kinking indicates that further development or evaluation of the criterion formulations is needed.

Fourth, the material modeling should be extended. Most simulations in this thesis were performed using homogeneous linear elastic material behavior. Although this is suitable for evaluating the basic performance of the VCTD formulations, it cannot capture residual plasticity, cyclic hardening, crack tip blunting or material-dependent fatigue mechanisms. Elastic-plastic simulations, preferably combined with cyclic plasticity models, should therefore be investigated further, especially for cases such as "RSB3" where the transition from shear mode to tensile mode growth may be material-dependent. Additionally, the influence of microstructural defects, such as inclusions and voids, should be considered, as these may affect crack initiation and subsequent crack propagation. Moreover, further sensitivity analyses should be carried out for the numerical implementation of the crack growth framework. In particular, for the Twin-Disc experiment, a sensitivity study of the evaluation distance (d_h) is required, as well as a sensitivity analysis of the contact load position on the top surface. These parameters may affect the local stress intensity factor extraction and the resulting predicted crack growth direction under rolling contact conditions.

Fifth, crack face interaction should be modeled in more detail. Crack face contact, friction, roughness, oxide formation and wear debris can influence both the effective sliding displacement and the crack growth rate. These effects are especially relevant for shear mode crack growth and rolling contact fatigue. Including frictional crack face contact and studying its sensitivity would improve the physical realism of the simulations.

Finally, future investigations would benefit from experiments performed in parallel with the numerical modeling. In the present thesis, several assumptions were required because the simulations were based on experiments reported in the literature. Dedicated experiments would allow the geometry, loading history, material parameters, crack path and crack growth rates to be measured in a way that is directly compatible with the numerical model. This would reduce modeling uncertainty and provide a stronger basis for validating both the VCTD direction criterion and the associated crack growth rate formulation.

Bibliography

[1] N. E. Dowling, S. L. Kampe, and M. V. Kral. *Mechanical Behavior of Materials*. Pearson Education, 2019.

[2] S. J. Findlay and N. D. Harrison. “Why aircraft fail”. In: *Materials Today* 5.11 (2002), pp. 18–25. DOI: 10.1016/S1369-7021(02)01138-0.

[3] S.-P. Zhu et al. “Probabilistic physics of failure-based framework for fatigue life prediction of aircraft gas turbine discs under uncertainty”. In: *Reliability Engineering & System Safety* 146 (2016). DOI: 10.1016/j.ress.2015.10.002.

[4] U. Zerbst, K. Mädler, and H. Hintze. “Fracture mechanics in railway applications—an overview”. In: *Engineering Fracture Mechanics* 72.2 (2005), pp. 163–194. DOI: 10.1016/j.engfracmech.2003.11.010.

[5] E. Magel. *Rolling contact fatigue: A comprehensive review*. 2011. DOI: 10.4224/23000318.

[6] P. Paris and F. Erdogan. “A critical analysis of crack propagation laws”. In: *Journal of Basic Engineering* 85 (1963). DOI: 10.1115/1.3656900.

[7] A.-H. I. Mourad et al. “Fatigue life and crack growth prediction of metallic structures: A review”. In: *Structures* 76 (2025), p. 109031. DOI: 10.1016/j.istruc.2025.109031.

[8] S. Khan, M. Junaid, and F. Khan. “Investigating the effect of crack inclination on strain energy and stress intensity under uniaxial loading”. In: *Engineering Proceedings* 23.1 (2022). DOI: 10.3390/engproc2022023009.

[9] J. Qian and A. Fatemi. “Fatigue crack growth under mixed-mode I and II loading”. In: *Fatigue & Fracture of Engineering Materials & Structures* 19.10 (1996). DOI: 10.1111/j.1460-2695.1996.tb00950.x.

[10] P. Zerres and M. Vormwald. “Review of fatigue crack growth under non-proportional mixed-mode loading”. In: *International Journal of Fatigue* 58 (2014). Fatigue Crack Paths 2012. DOI: 10.1016/j.ijfatigue.2013.04.001.

[11] S. T. Hengeveld et al. “Crack path under non-proportional fatigue loading—Evaluating tests with existing crack growth direction criteria”. In: *Theoretical and Applied Fracture Mechanics* 141 (2026), p. 105069. DOI: 10.1016/j.tafmec.2025.105069.

[12] S. L. Wong et al. “A branch criterion for shallow angled rolling contact fatigue cracks in rails”. In: *Wear* 191.1 (1996). 4th International Conference on Contact Mechanics and Wear of Rail-Wheel Systems. DOI: 10.1016/0043-1648(95)06621-7.

[13] C. Li. “Vector CTD criterion applied to mixed-mode fatigue crack growth”. In: *Fatigue & Fracture of Engineering Materials & Structures* 12.1 (1989). DOI: 10.1111/j.1460-2695.1989.tb00508.x.

[14] BETA CAE Systems. *ANSA Pre-Processor, Version 23.1.1.* Switzerland: BETA CAE Systems, 2022.

[15] Dassault Systèmes Simulia Corp. *Abaqus/Standard User’s Manual, Version 2022*. United States, 2022.

[16] The MathWorks Inc. *MATLAB version 9.13.0 (R2022b).* Natick, MA, USA: The MathWorks Inc., 2022.

[17] D. Floros, A. Ekberg, and F. Larsson. “Evaluation of crack growth direction criteria on mixed-mode fatigue crack growth experiments”. In: *International Journal of Fatigue* 129 (2019), p. 105075. DOI: 10.1016/j.ijfatigue.2019.04.013.

[18] M. Salahi Nezhad et al. “Numerical prediction of railhead rolling contact fatigue crack growth”. In: *Wear* 530–531 (2023), p. 205003. DOI: 10.1016/j.wear.2023.205003.

[19] G. R. Irwin. “Analysis of stresses and strains near the end of a crack traversing a plate”. In: *Journal of Applied Mechanics* 24 (1957). DOI: 10.1115/1.4011547.

[20] H. Yu and M. Kuna. “Interaction integral method for computation of crack parameters K–T—A review”. In: *Engineering Fracture Mechanics* 249 (2021), p. 107722. DOI: 10.1016/j.engfracmech.2021.107722.

[21] S. L. Wong et al. “Fatigue crack growth rates under sequential mixed-mode I and II loading cycles”. In: *Fatigue & Fracture of Engineering Materials & Structures* 23 (2000). DOI: 10.1046/j.1460-2695.2000.00342.x.

[22] P. Wriggers. *Computational Contact Mechanics*. Springer Dordrecht, 2006. DOI: 10.1007/978-3-540-32609-0.

[23] K. Tanaka. “Fatigue crack propagation from a crack inclined to the cyclic tensile axis”. In: *Engineering Fracture Mechanics* 6.3 (1974). DOI: 10.1016/0013-7944(74)90007-1.

[24] Z. Ding et al. “Modeling of I+II mixed-mode crack initiation and growth from the notch”. In: *Theoretical and Applied Fracture Mechanics* 84 (2016). DOI: 10.1016/j.tafmec.2016.03.011.

[25] Z. Ding et al. “An experimental investigation and prediction of fatigue crack growth under overload/underload in Q345R steel”. In: *International Journal of Fatigue* 98 (2017), pp. 155–166. DOI: 10.1016/j.ijfatigue.2017.01.024.

[26] P. E. Bold. “Multiaxial fatigue crack growth in rail steel”. Ph.D. thesis. Sheffield, U.K., 1990.

[27] E. W. Smith and K. J. Pascoe. “The behaviour of fatigue cracks subject to applied biaxial stress: A review of experimental evidence”. In: *Fatigue & Fracture of Engineering Materials & Structures* 6.3 (1983). DOI: 10.1111/j.1460-2695.1983.tb00338.x.

[28] D. I. Fletcher and J. H. Beynon. “The influence of lubricant type on rolling contact fatigue of pearlitic rail steel”. In: *Lubrication at the Frontier*. Vol. 36. Tribology Series. Elsevier, 1999. DOI: 10.1016/S0167-8922(99)80051-0.

[29] H. Hertz. “Ueber die Berührung fester elastischer Körper”. In: *Journal für die reine und angewandte Mathematik* 1882.92 (1882), pp. 156–171. DOI: 10.1515/crll.1882.92.156.

[30] K. L. Johnson. *Contact Mechanics*. Cambridge University Press, 1985.

[31] M. Salahi Nezhad et al. “Numerical predictions of crack growth direction in a railhead under contact, bending and thermal loads”. In: *Engineering Fracture Mechanics* 261 (2022), p. 108218. DOI: 10.1016/j.engfracmech.2021.108218.

[32] A. Skyttebol, B. L. Josefson, and J. W. Ringsberg. “Fatigue crack growth in a welded rail under the influence of residual stresses”. In: *Engineering Fracture Mechanics* 72.2 (2005). Fracture Mechanics in Railway Applications, pp. 271–285. DOI: 10.1016/j.engfracmech.2004.04.009.

DEPARTMENT OF MECHANICAL ENGINEERING
CHALMERS UNIVERSITY OF TECHNOLOGY
Gothenburg, Sweden
www.chalmers.se

CHALMERS
UNIVERSITY OF TECHNOLOGY